JGR Solid Earth

RESEARCH ARTICLE
10.1029/2018JB016451

Azimuthal Seismic Anisotropy of 70-Ma Pacific-Plate Upper Mantle

H. F. Mark[1,2], D. Lizarralde[2], J. A. Collins[2], N. C. Miller[3], G. Hirth[4], J. B. Gaherty[5], and R. L. Evans[2]

[1]MIT/WHOI Joint Program in Oceanography/Applied Ocean Science and Engineering, Woods Hole, MA, USA, [2]Department of Geology and Geophysics, Woods Hole Oceanographic Institution, Woods Hole, MA, USA, [3]U.S. Geological Survey, Reston, VA, USA, [4]Geological Sciences Department, Brown University, Providence, RI, USA, [5]Lamont-Doherty Earth Observatory of Columbia University, Palisades, NY, USA

Key Points:
- We measure 6.0 ± 0.3% anisotropy at the Moho in 70-Ma oceanic lithosphere, increasing to ~7.7% at 7 km below the Moho
- The increase in anisotropy with depth suggests the presence of an extrinsic source of anisotropy, such as oriented cracks
- The fast direction is along 83 ± 1°N, parallel to paleospreading

Correspondence to:
H. F. Mark,
hmark@whoi.edu

Citation:
Mark, H. F., Lizarralde, D., Collins, J. A., Miller, N. C., Hirth, G., Gaherty, J. B., & Evans, R. L. (2019). Azimuthal seismic anisotropy of 70-Ma Pacific-plate upper mantle. *Journal of Geophysical Research: Solid Earth*, *124*, 1889–1909. https://doi.org/10.1029/2018JB016451

Received 24 JUL 2018
Accepted 20 JAN 2019
Accepted article online 28 JAN 2019
Published online 16 FEB 2019

Abstract Plate formation and evolution processes are predicted to generate upper mantle seismic anisotropy and negative vertical velocity gradients in oceanic lithosphere. However, predictions for upper mantle seismic velocity structure do not fully agree with the results of seismic experiments. The strength of anisotropy observed in the upper mantle varies widely. Further, many refraction studies observe a fast direction of anisotropy rotated several degrees with respect to the paleospreading direction, suggesting that upper mantle anisotropy records processes other than 2-D corner flow and plate-driven shear near mid-ocean ridges. We measure 6.0 ± 0.3% anisotropy at the Moho in 70-Ma lithosphere in the central Pacific with a fast direction parallel to paleospreading, consistent with mineral alignment by 2-D mantle flow near a mid-ocean ridge. We also find an increase in the strength of anisotropy with depth, with vertical velocity gradients estimated at 0.02 km/s/km in the fast direction and 0 km/s/km in the slow direction. The increase in anisotropy with depth can be explained by mechanisms for producing anisotropy other than intrinsic effects from mineral fabric, such as aligned cracks or other structures. This measurement of seismic anisotropy and gradients reflects the effects of both plate formation and evolution processes on seismic velocity structure in mature oceanic lithosphere, and can serve as a reference for future studies to investigate the processes involved in lithospheric formation and evolution.

1. Introduction

The structure of mature oceanic lithosphere derives from plate formation processes at mid-ocean ridges combined with off-axis modification as the plate ages. The composition of the lithosphere is derived from melting of the upper mantle at mid-ocean ridges. Some mantle minerals preferentially melt and are extracted at the ridge to form the crust, while other minerals remain in the residual lithospheric mantle. Lab-based melting models predict that this will result in a compositional gradient from lherzolite at depth up to depleted harzburgite in the shallowest mantle (e.g., Langmuir et al., 1992), and evidence for such a gradient is seen in peridotite samples from seafloor dredges and ophiolites (e.g., Constantin et al., 1995; Dick et al., 1984; Kelemen et al., 1992; Ringwood, 1958). Ridge processes also produce mineral fabrics in the lithosphere. The mantle experiences large shear strains during corner flow at the ridge, and laboratory experiments show that this can impart an anisotropic fabric that can be locked into the lithospheric mantle as minerals are aligned into a crystallographic preferred orientation (CPO) by shear (e.g., Nicolas et al., 1973; Turner, 1942; Zhang & Karato, 1995). Off-axis, plate structure continues to evolve: as plates cool, they undergo tensional cracking and serpentinization (e.g., Cormier et al., 2011; Dunn, 2015; Korenaga, 2007; Mishra & Gordon, 2016; Sandwell & Fialko, 2004).

Our current understanding of plate formation and evolution processes, and the relationships between physical properties and seismic velocities, enable us to make predictions about the seismic velocity structure of oceanic lithosphere including seismic anisotropy and vertical gradients. The vertical velocity gradient in the uppermost oceanic mantle is predicted to be negative (e.g., Stixrude & Lithgow-Bertelloni, 2005) as the effects on seismic velocities due to compositional gradients resulting from melt extraction (Langmuir et al., 1992) and thermal gradients established by plate cooling (e.g., Christensen, 1979) are stronger than the effect of increasing pressure with depth (O. L. Anderson et al., 1968; Greenfield & Graham, 1996; Meglis et al., 1996). For dominantly two-dimensional (2-D) mantle flow, the alignment of anisotropic

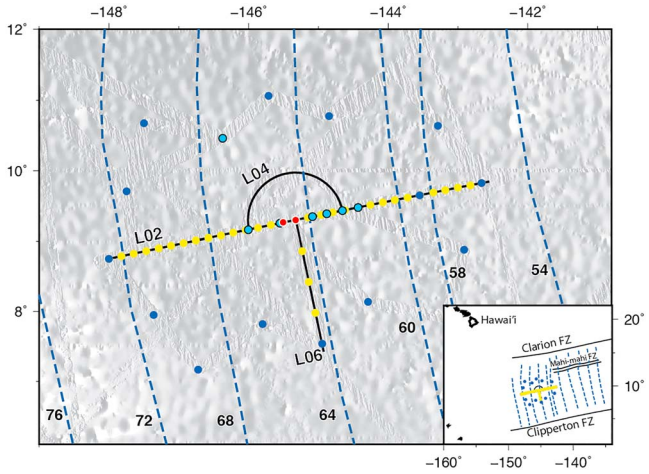

Figure 1. Map of the central Pacific showing the NoMelt array. Short-period (SP) OBS are marked by yellow dots and broadband (BB) OBS by blue dots. Lighter blue dots outlined in black indicate BB instruments used in this study. SP OBS A15 and BB OBS B14 (Figures 3 and 10) are marked by red dots outlined in white. Shotlines are in black: L02 runs nearly east-west, L06 runs nearly north-south, and L04 is a semicircle near the center of the array. Dashed light blue lines show isochrons from Barckhausen et al. (2013) and the bathymetry is from GMRT v3.4 (Ryan et al., 2009). The inset map shows the location of the array within the Pacific. The study site is located between the Clarion and Clipperton fracture zones, approximately 1,500 km southeast of Hawai'i.

olivine crystals into a CPO is expected to produce seismic anisotropy in the lithospheric mantle such that *P* wave velocities are fastest for seismic waves propagating parallel to the direction of plate spreading (Hess, 1964; Mainprice, 2015; Skemer & Hansen, 2016; Turner, 1942; Verma, 1960; Zhang & Karato, 1995). The azimuth along which *P* wave velocities are largest is referred to as the fast direction of anisotropy. If aligned cracks are present due to off-axis cooling, they are also predicted to produce anisotropy as velocities are slowed normal to the cracks (e.g., D. L. Anderson et al., 1974; Hudson, 1981; Nishizawa, 1982).

Seismic observations have shown that anisotropy is indeed present throughout the oceanic upper mantle, but other aspects of these predictions for lithospheric velocity structure are either unverified by or in conflict with observations. The fact that strong *Pn* phases are seen in seismic refraction experiments requires that positive velocity gradients exist in at least some parts of the oceanic upper mantle, contrary to predictions from physical models. Anisotropy consistent with a CPO formed by 2-D mantle flow has been measured at some locations in the oceanic upper mantle (Raitt et al., 1969; Shimamura, 1984; Snydsman et al., 1975), but many refraction studies measure anisotropy where the fast direction is not parallel to the paleospreading direction, suggesting that 3-D mantle flow patterns and/or other processes that influence lithospheric anisotropy may be relatively common (Dunn & Toomey, 1997; Keen & Barrett, 1971; Keen & Tramontini, 1970; Morris et al., 1969; Shearer & Orcutt, 1986; Shintaku et al., 2014; Toomey et al., 2007; VanderBeek et al., 2016; VanderBeek & Toomey, 2017). Further, estimates of the strength of anisotropy vary widely (e.g., Gaherty et al., 2004; Shimamura, 1984).

The lack of consistency among observations of anisotropy and differences between observed and predicted velocity structures raise questions about the processes involved in lithospheric formation and evolution. It is not clear whether the anisotropy we observe is set primarily by mantle corner flow during plate formation, or if plate evolution processes, such as cracking and chemical alteration, contribute significantly to the signal. Azimuthal anisotropy is often discussed as a product of 2-D mantle flow, but the role of 3-D flow patterns at mid-ocean ridges and their effects on anisotropic fabric in the lithosphere are not well understood. Resolving these questions requires a baseline of observations in oceanic lithosphere from a simple setting where we expect the links between plate formation and evolution processes and the observed seismic structure to be relatively straightforward.

We present a measurement of upper mantle anisotropy and vertical velocity gradients in 70-Ma lithosphere in the central Pacific using active-source refraction data acquired during the 2011 NoMelt experiment. This measurement can serve as a reference model for upper mantle anisotropy, and provides a point of comparison for future, targeted studies of anisotropy in oceanic lithosphere. We find that the magnitude of anisotropy increases with depth. The depth variation suggests that the effective anisotropy includes some extrinsic component, such as anisotropy due to aligned or spatially organized cracks.

2. The NoMelt Experiment and Data

The NoMelt experiment was conducted in 2011–2012 on ~70-Ma lithosphere between the Clarion and Clipperton fracture zones in the central Pacific (Figure 1) and was designed to image the detailed seismic and electrical structure of "normal," mature oceanic lithosphere and the underlying asthenosphere. Normal here refers to lithosphere with a simple evolutionary history, where the effects of processes involved in plate formation and evolution should be minimally overprinted by the effects of more complex tectonics. At an age of 70 Ma the plate is no longer directly influenced by ridge processes, and at this particular site there is no evidence for modification of the lithosphere since its formation by, for example, hot spot volcanism. The estimated paleospreading half-rate at this location is intermediate at 35 mm/year (Barckhausen et al., 2013).

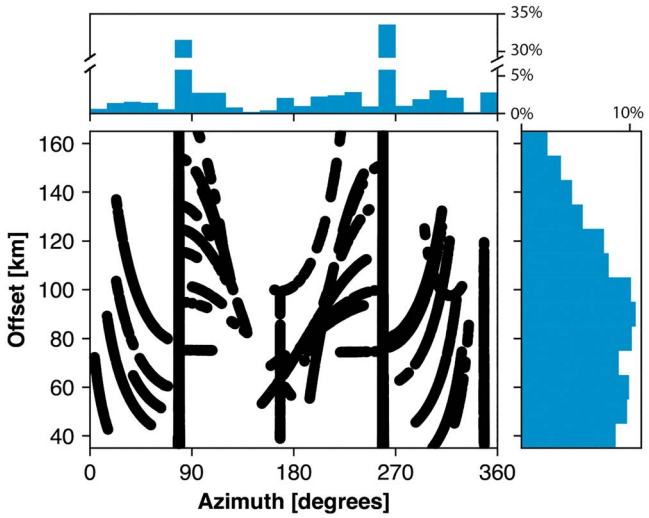

Figure 2. Distributions of source–receiver offset and azimuth for the 7,961 travel time picks (black) used in the analyses. Histograms show (top) the uneven distribution of azimuths and (right) the more uniform distribution of offset in the data set.

The seismic component of NoMelt consisted of a 600 × 400-km array of 26 broadband (BB) ocean-bottom seismometers (OBS), 22 of which were recovered, and 34 short-period (SP) OBS, 33 of which were recovered. The SP instruments were deployed at 20-km intervals along Line 02 (L02), the main active-source transect striking at an azimuth of ~78.5°N, parallel to the plate-kinematic flow line, and at 50-km intervals along Line 06 (L06), a 200-km line normal to the center of the main transect (Figure 1). The OBS array recorded air gun shots fired by the R/V *M.G. Langseth's* 36-element array. Shots were fired along L02, L06, and Line 04 (L04), a semicircle with radius 75 km centered at the intersection of L02 and L06. A shot interval of 4 min was used to ensure that previous shot noise did not obscure refraction arrivals at large offsets. The source geometry was designed to provide large-offset refraction data along L02, good controls on velocities parallel and perpendicular to the plate kinematic flow line with L02 and L06, and full azimuthal coverage with L04.

Broadband data from NoMelt have been used to constrain shear wave velocity and anisotropy in the upper mantle down to 300 km (Lin et al., 2016; Russell et al., 2019). Lin et al. (2016) observe the strongest anisotropy in the shallowest part of their model (G parameter ~2.5%), with the fast direction approximately parallel to paleospreading. They attribute the shallow anisotropy to high strain in the lithospheric mantle during corner flow and plate spreading, and propose that anisotropy deeper in the asthenosphere could result from pressure-gradient-driven return flow or density-driven small-scale convection beneath the plate. In this study, we present a measurement of P wave anisotropy within the upper ~7 km of the mantle.

3. Methods and Results

We estimate azimuthal anisotropy in the upper ~7 km of the mantle using a delay-time approach (e.g., Raitt et al., 1969). Delay times are the differences between observed travel times of mantle refractions (*Pn*) and times predicted for propagation through an isotropic mantle. These differences are interpreted as the effect of anisotropic wave speeds in the upper mantle. We calculate the delay times and model them in terms of anisotropic elasticity parameters.

The calculation of delay times from observed *Pn* travel times involves accounting for two main travel time effects separate from the effects of anisotropy: effects unrelated to mantle propagation (static effects) and effects due to both azimuthal variation in travel time through an isotropic 1-D crust and variable propagation distances within the mantle (propagation effects). The dominant static effect is due to variable water depth. High-quality swath bathymetry data collected during the NoMelt survey are used to correct for water depth variations. Correcting for propagation effects is done using ray-tracing methods, but the correction relies on estimates of mantle velocity at different azimuths. This means that calculating the delay times used to determine the anisotropic velocities requires prior knowledge of the azimuthal velocity variation, making the measurement of azimuthal anisotropy from refraction data a nonlinear problem. We address this nonlinearity by solving the problem with an iterative approach, described below, beginning with an initial estimate of azimuthal velocity variation determined directly from the data. This initial estimate is obtained by fitting travel time as a function of source–receiver offset. The offset dependence of travel time at a given azimuth also provides sensitivity to the azimuthal variation of vertical velocity gradients. We incorporate gradients into the propagation correction and use a grid-search method to find a preferred model for vertical velocity gradients along with the anisotropy model.

We analyzed 7,961 refraction travel times observed at 31 OBS from shots along L02, L04, and L06. The travel times were picked by hand, as opposed to with an automatic picking algorithm. The majority of the picks (64%) are from along L02 at azimuths near 79°N and 259°N (Figure 2). About 64% of picks are at source–receiver offsets between 35 and 100 km with the distribution peak at 90 km, and 36% are between 100 and 165 km (Figure 2). We show that an inversion of synthetic travel times with the same offset and azimuthal distributions as the NoMelt data recovers a known velocity model equally well as data that have a uniform

distribution of azimuth and offset. However, binning tests indicate that the uneven distribution of azimuths in the data skews our inversion, so we devise a weighting scheme to mitigate the effects of the data distribution.

The following sections describe the steps outlined above, including the application of static corrections, the initial estimate of azimuthal anisotropy, and the iterative application of propagation corrections and linear inversion for azimuthal anisotropy. The inversion is done with two parameterizations: one with no vertical velocity gradients and one with vertical gradients that can vary by azimuth. We present the results alongside the methods to demonstrate the effect of each step in the process, and because the methodology depends on the results in important ways. In particular, we present inversions of azimuthally binned versus unbinned data, and the resulting models have slightly different fast direction orientations, suggesting that the large amount of data along L02 leverages the fast direction estimate. We therefore also present the results of inversions where the data along the L02 azimuth and back azimuth are downweighted. The end result is three pairs of models: one based on all of the travel time data equally weighted, one based on azimuthally binned data, and one based on the data with L02 travel times downweighted. The six models are slightly different from one another but are equally valid, and we describe the implications of those differences for our preferred final model.

3.1. Data Processing and Reduction

Processing steps for the OBS data included band-pass filtering, deconvolution, OBS relocation, and, for the BB OBS, resampling. The data were filtered using an eight-pole, minimum-phase Butterworth filter with corner frequencies of 4 and 15 Hz to increase the signal-to-noise ratio of the *Pn* phase, which has a dominant frequency of ~10 Hz. A linear prediction deconvolution with a filter length of 0.2 s and a prediction distance of 0.01 s was applied using the software package *SIOSEIS* (Henkart, 2003) to attenuate reverberations from shallow structure. The SP OBS recorded at 200 samples per second, and the BB OBS at 50 samples per second. The BB OBS were resampled to 5 ms to aid in picking.

The seafloor locations of the SP OBS were determined using direct water wave arrival times and a grid-search centered on the OBS deployment locations. For each OBS, predicted travel times for the direct water wave were calculated for a grid of positions surrounding the deployment location, with the depth at each position taken from the multibeam bathymetry grid. At each grid point location, the root-mean-square error (RMSE) of the predicted travel times was calculated with respect to the observed travel times. This constrained the instrument location to within the set of positions where the RMSE was less than or equal to the uncertainty of the observed travel times. The seafloor location was chosen as the position in that set closest to the sea-surface deployment location. Each estimated seafloor OBS location was less than 600 m away from its corresponding deployment location. The BB OBS were located by ranging to the instruments from several azimuths using 12-kHz acoustic signals.

Travel time data were obtained by hand-picking *Pn* first arrivals on the vertical ground-motion components of 23 SP and 8 BB OBS. Where corresponding pairs of sources and receivers were available, travel times were checked for reciprocity. The travel time picks covered 360° of azimuth across the center of the array (Figure 2). The azimuthal distribution of data at offsets greater than 165 km is sparse. We therefore chose to use only picks with source–receiver offsets up to 165 km in the analysis for anisotropy. In addition, we do not use picks from shots along the western 180 km of L02. For shots along the eastern 420 km of L02, OBS receiver gathers show a pattern of horizontal phase velocity of the *Pn* branch out to ~250 km that is similar for all instruments, indicative of a mostly 1-D uppermost mantle velocity structure. This pattern changes abruptly 180 km from the western end of L02, near the location indicated in Figure 3. The *Pn* refraction phase observed over the western portion of L02 has a horizontal phase velocity that is variable and generally greater than in the east, indicative of some amount of variable uppermost mantle structure west of km 180. The change that occurs across km 180 presumably reflects a relatively minor transient event that occurred at the ridge, such as the propagation of a ridge discontinuity, since there are no dramatic bathymetric or crustal-scale features marking this location.

3.2. Static Corrections

Static time corrections were applied to the data to correct for the effects of variable water depth and sediment thickness on travel times. Although the NoMelt site has a relatively thin sediment cover (~200 m) and low

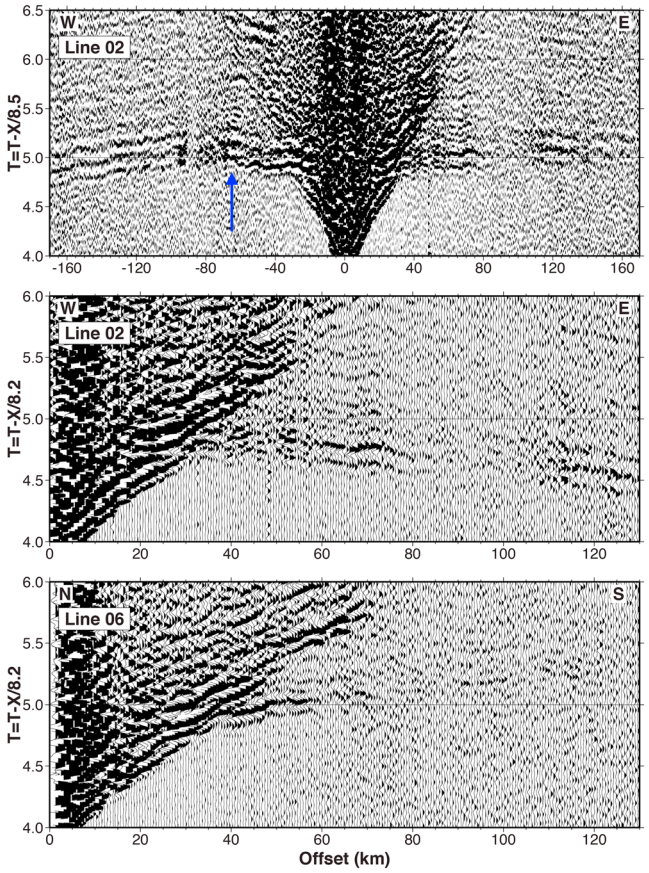

Figure 3. Record sections corrected for variable water depth and sediment thickness for BB OBS B14, located at the crossing of L02 and L06. Data from shots along L02 are shown in the top two panels; the bottom panel shows data from shots along L06. A blue arrow in the top panel indicates the transition to faster phase velocities 180 km from the western end of L02. The horizontal phase velocity of *Pn* is observed to be greater than 8.2 km/s along L02, the flow-line direction, and slower than 8.2 km/s perpendicular to the flow line along L06.

topographic relief, these time corrections are important for our measurement because the travel time signal from azimuthal anisotropy is small. Water depth along the shot lines varied by ~300 m, and for a standard water velocity of 1.5 km/s, a 300-m increase in water depth adds approximately 200 ms of travel time unrelated to mantle velocity structure. A similar effect is seen for variations in sediment thickness on both the source and receiver sides of the raypath. This is a significant time contribution relative to that of anisotropy: for comparison, in a medium with 7% anisotropy, similar to what has been previously observed in the Pacific (Keen & Barrett, 1971; Morris et al., 1969; Raitt et al., 1969), the travel time difference between the fast and slow directions for a mantle refraction at 75 km is only ~800 ms.

The static corrections were calculated based on high-resolution swath bathymetry and multichannel seismic (MCS) data. MCS data from L02 and L06 were stacked and time-migrated using Paradigm Geophysical's *Echos* software. The travel time to the basement was picked on the migrated sections and those travel times were used along with bathymetry data to estimate sediment thickness along L02 and L06. To calculate source-side statics, we used a ray parameter of 1/8.5 s/km to find the piercing points at which each downgoing ray intersects the seafloor and basement. Travel times through the water and sediments were estimated based on the piercing points using a constant water velocity of 1.5 km/s and sediment velocity of 1.8 km/s, and those times were subtracted from travel times calculated for a uniform water depth of 5,175 m and a uniform sediment thickness of 120 m to obtain the source-side static corrections. Receiver-side statics were also calculated based on 120-m-thick sediments, assuming a vertical upgoing ray through the sediments. Since all of the OBS were located along L02 and L06, receiver-side statics were applied to all travel time picks. However, the L04 MCS data could not be satisfactorily migrated, so the L04 source-side statics corrected for variable water depth but not for sediment thickness. The static corrections were on the order of 50–100 ms. The static corrections were applied to the OBS data before picking travel times because removing the effects of bathymetry and sediments on the source side greatly improved phase coherence for *Pn*.

3.3. Propagation Corrections

Calculating delay times from picked and static-corrected *Pn* travel times involves accounting for the travel time contributions from two propagation effects: variable propagation distance through the mantle and azimuthal variation in crustal propagation times. The *Pn* delay time is the difference between the observed travel time of a *Pn* phase that has propagated some distance through the mantle, and the predicted travel time for propagation through an isotropic mantle over the same distance. Since the time delay with respect to travel time in an isotropic mantle accrues along the raypath, the magnitude of the delay time depends on the mantle propagation distance, and this dependency must be accounted for in order to use the variation of delay times with azimuth to estimate anisotropic parameters. The NoMelt *Pn* travel time data span a range of source–receiver offsets (Figure 2) and thus a range of mantle propagation distances. Further, these travel times include propagation times through the crust, which also vary with azimuth if the mantle is anisotropic. This is true even when the crustal velocity structure is isotropic because the horizontal propagation distance in the crust depends on the critical angle for refraction, which in turn depends on the velocity at the top of the mantle.

We use ray tracing to estimate the propagation effects and subtract those effects from the static-corrected travel times. For each pick, the full offset was traced through a water layer, sediment, crust, and mantle in a model with an anisotropic mantle, using the mantle velocity corresponding to the pick azimuth. Velocity

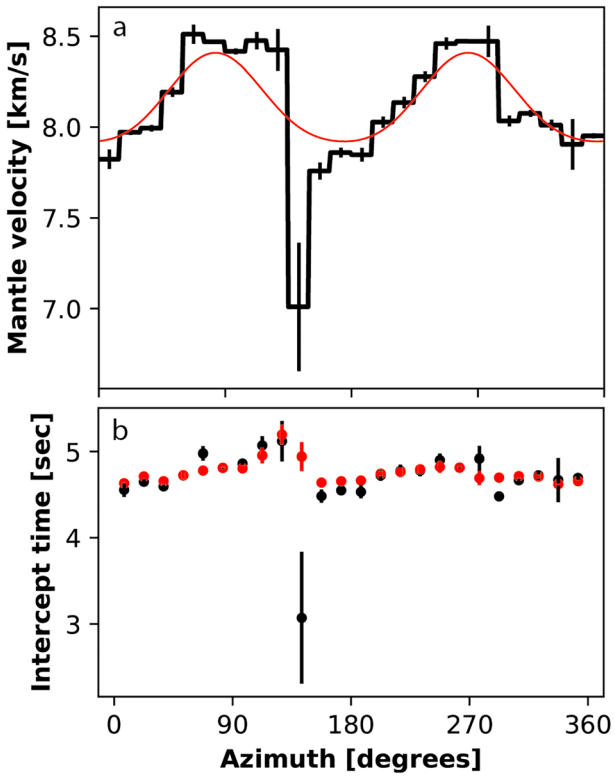

Figure 4. (a) Bin velocities used for the initial iteration of the joint propagation correction and model inversion (black) and the final model obtained after the iterations converged (red). Black bars show the 95% confidence intervals for the bin velocities. The anomalous bin velocity near 140°N is due to a sparsely populated bin with only 16 picks constraining the linear fit. (b) Intercept times from the initial bin velocity model (black), and intercept times calculated from the final model, which has a constant crustal thickness (red). The close agreement between these intercept times indicates that the variation in intercept times is primarily due to the mantle anisotropy and that crustal thickness variations throughout the NoMelt region are small.

depth gradients in the mantle were set as a function of azimuth. The choice of gradients is discussed further in section 3.5. At the same azimuth, and with identical water, sediment, and crustal layers, a ray was traced such that it traveled a set reference distance horizontally in the mantle. The propagation correction is the difference between the traced time at the full distance, and the traced time at the reference mantle propagation distance. Algebraically, we can write the propagation correction T_{corr} as

$$T_{\mathrm{corr}} = T_{M,\mathrm{ref}} - T_{M,X} - T_{C,X} \tag{1}$$

where $T_{M,\ \mathrm{ref}}$ is the traced traveltime in an anisotropic mantle for the reference distance and $T_{M,\ X}$ and $T_{C,\ X}$ are the traced travel times in the anisotropic mantle and the crust, respectively, for the true source–receiver offset. Subtracting the propagation correction from the observed travel time accounts for time spent traversing the crust as well as the difference in mantle travel time due to source–receiver offset.

The delay time dT is calculated as

$$dT = T_{\mathrm{obs}} - T_{\mathrm{corr}} - T_{M,\mathrm{iso}} \tag{2}$$

where T_{obs} is the observed total travel time and $T_{M,\ \mathrm{iso}}$ is the traced travel time in an isotropic mantle for the reference distance. This produces a set of delay times that are referenced to the chosen reference distance for horizontal mantle propagation. The average horizontal distance that a NoMelt *Pn* phase traveled through the water column, sediments, and crust is ~16 km, so a reference mantle propagation distance of 75 km is used such that the total average reference offset is 91 km, matching the peak of the distribution of source–receiver offsets in the data (Figure 2).

Uncertainty in the delay times could come from three main sources: the lack of sediment source-side statics along L04, uncertainty in OBS locations propagated through the propagation correction, and picking error. The contribution from the L04 sediment statics should be very small since the combined source- and receiver-side static corrections were generally under 100 ms in total. The uncertainty in instrument positions is likely to be small after relocation compared to total source–receiver offsets, and we do not observe coherent shifts in the residuals by station indicative of large location errors. The contribution from picking error is likely to be similar across the data set since picks are made with consideration for the correlation between arrivals on adjacent traces. Here we assume that all of our picks have the same uncertainty.

Calculating the propagation corrections requires a model of the anisotropic mantle velocity structure, so the determination of the propagation corrections and the model of mantle velocity structure are done together in an iterative inversion. The initial velocity model for the propagation correction was determined by binning the travel time data into 15° azimuthal bins and fitting a line to the travel times versus offset within each bin. The slopes of these lines were used as an initial estimate of velocity within each azimuthal bin (Figure 4). The bin velocities indicate a clear azimuthal variation in wave speed. The initial propagation correction was calculated by ray tracing through the piecewise bin velocity model described above.

The intercept times of the lines fit to the binned travel time data were used to constrain the crustal portion of the model for the propagation correction. The intercept time, which represents the vertical component of propagation through water, sediments, and crust, is proportional to the product of twice the crustal thickness times the vertical slowness at the critical angle for refraction. That critical angle is a function of the velocity at the top of the mantle. The horizontal component of crustal propagation also depends on the critical angle, and these dependencies introduce an azimuthal variation into the crustal propagation times of the *Pn* phase for an anisotropic mantle even when the crust itself is isotropic. We used the proportionality between the intercept time and crustal thickness to determine the crustal velocity model. Using a water

depth of 5,175 m and sediment thickness of 120 m based on MCS and multibeam bathymetry data from the NoMelt site, and setting the top mantle velocity as the average of the bin velocities, we calculated intercept times for different assumed thicknesses of oceanic crustal layers 2 and 3. The two crustal layer thicknesses were taken to be equal, and the crustal velocities were based on a typical 1-D velocity model (e.g., Bratt & Purdy, 1984; Fowler, 2005). These predicted intercept times were compared to the average intercept time for the data, and the best fitting layer thickness was approximately 3 km, giving an overall crustal thickness of 6 km. This crustal model was used in all ray tracing. We chose to use an isotropic crustal model because the travel time residuals due to crustal azimuthal anisotropy are small (~30 ms; Dunn, 2015) relative to the contributions from mantle anisotropy, especially for mantle refractions which only propagate a short distance in the crust. The mean horizontal distance traveled in the crust, sediment, and water column was ~16 km, corresponding to ~6.5 s of travel time.

We used two different model parameterizations in the inversion for mantle anisotropy. Both parameterizations include the crustal model described above. The parameterizations differ in the velocity gradient with depth through the mantle, with one parameterization having no vertical velocity gradient and the other having a positive gradient that varies with azimuth. We consider the parameterization with positive gradients because the *Pn* mantle refraction phase is observed to offsets of 350 km with strong amplitudes at many azimuths, and this implies that positive vertical velocity gradients with depth exist in the mantle. In addition, the amplitudes of the *Pn* phase are larger in the fast direction than in the slow direction, suggesting that the vertical velocity gradients vary with azimuth (e.g., Garmany, 1981). Azimuthally varying vertical velocity gradients are parameterized in the model as a sinusoidal variation over 90° (i.e., $\cos(2\theta)$) from a maximum value in the fast direction to a minimum value in the slow direction. As described below, the maximum and minimum values are not determined within the inversion for anisotropic parameters, but instead are found through a grid search over many individual inversion results.

3.4. Delay Times and Inversion for Anisotropy Parameters

The delay time can be written as $dT = r/dV$, where r is the propagation distance. After applying the propagation correction to bring the data to a common mantle propagation distance of 75 km, dV values were calculated from dT by evaluating

$$dV_i = \left(\frac{dT_i}{r} + \frac{1}{V_0}\right)^{-1} - V_0 \tag{3}$$

where the subscript i refers to the i^{th} travel time observation, r is the reference mantle propagation distance (75 km), and V_0 is the isotropic mantle velocity to which we are comparing the travel time data.

It has been shown that small azimuthal anisotropy in P wave velocity can be described by the functional form

$$dV \approx A + B\cos 2\theta + C\sin 2\theta + D\cos 4\theta + E\sin 4\theta \tag{4}$$

where dV is the variation in velocity with respect to an isotropic model and the coefficients A, B, C, D, and E are functions of the elastic parameters of the material (Backus, 1965; Crampin, 1984). In matrix form, this can be written as

$$\overrightarrow{dV} = K\overrightarrow{m} \tag{5}$$

where $\overrightarrow{dV}$ is a column vector of velocity variations, $\overrightarrow{m}$ is a vector containing the coefficients of equation (4), and K is the Jacobian relating the model parameters to the velocity variations:

$$K = \left[\left(\overrightarrow{1}\right)\left(\cos 2\overrightarrow{\theta}\right)\left(\sin 2\overrightarrow{\theta}\right)\left(\cos 4\overrightarrow{\theta}\right)\left(\sin 4\overrightarrow{\theta}\right)\right] \tag{6}$$

where $\overrightarrow{\theta}$ is a column vector of source–receiver azimuths and K has five columns and N rows for N travel time observations. Velocity variations dV were fit to the model in equation (4) using linear least squares.

Since a velocity model is used to calculate the propagation correction, if the velocity model obtained by the inversion (equation (4)) differs from the model used to correct the data, the model obtained from inversion is no longer consistent with the data. We therefore used an iterative approach to refine the velocity model until

a self-consistent model was obtained. Beginning with the piecewise bin velocity model, the procedure for iteration was as follows: (1) calculate the mean velocity from the current velocity model to use as the isotropic reference for the mantle; (2) find the fast-direction azimuth for the current velocity model to set the phase of the gradient model; (3) calculate the propagation correction and delay times using the current velocity model, gradients, and isotropic reference; and (4) calculate dV and invert for a new velocity model. This process was repeated using successive refinements of the velocity model until the model parameters did not appreciably change with subsequent iterations. The parameters changed very little after 5 iterations, and 10 iterations were completed to ensure convergence of the model.

Four separate inversion results, based on all of the travel time data, are shown in Figure 5. The largest difference between these models is between Figures 5a and 5b, where propagation corrections were made using the bin velocities in both cases but static corrections are applied only in Figure 5b, resulting in a substantially better fit to the data. The models in Figures 5a and 5b do not include iteration, so they are not self-consistent in the sense that the mantle velocities used to make the propagation corrections differ from the mantle velocities resulting from the inversion. The model in Figure 5c results from 10 iterations where propagation corrections are iteratively refined and the inversion is repeated until a self-consistent model is obtained. This reduces the percent anisotropy from 6.6% to 6.5% and increases the RMSE from 65 to 67 ms. Models in Figures 5a–5c are inversion results using the parameterization without gradients. The model in Figure 5d includes azimuthally varying vertical velocity gradients. The fit of this model, with RMSE of 65 ms, is improved over Figure 5c, and the model has a lower anisotropy at the Moho of 6.3%.

The models shown in Figures 5b–5d are quite similar, both visually and quantitatively. The similarity between Figures 5b and 5c reflects how close the bin velocity model is to the continuous model obtained by inversion. Although incorporating the gradient parameterization does not result in significant changes in Figure 5d compared to Figure 5c, systematic variation in *Pn* amplitudes with azimuth suggests that the gradient parameterization is a better representation of the velocity structure. The choice of gradient values is discussed further in the next section.

3.5. Vertical Velocity Gradients

Vertical velocity gradients were estimated using a grid-search over the two values that we use to parameterize the azimuthal variation of velocity gradient: the gradients in the fast and slow directions. We performed a complete inversion, from initial tracing with the bin velocities through successive iterative refinement, for pairs of fast- and slow-direction gradients over a grid. RMSE was calculated for each inversion, and the preferred pair of gradient values was chosen based on the minimum RMSE.

Results of the grid-search used to determine the preferred gradient parameters are summarized in Figure 6. Our preferred gradient model has gradients of 0.02 km/s/km in the fast direction and 0 km/s/km in the slow direction. The absolute minimum RMSE is found for a slow-direction gradient of 0.01 km/s/km, with an RMSE value 0.002 ms lower than that of the preferred model. However, synthetic tests discussed in the next section showed that the NoMelt data distribution can only weakly resolve the slow-direction gradient, so this was not considered sufficient evidence for a strong slow-direction gradient. Further, the low amplitudes of *Pn* arrivals along the slow direction (Figure 3) support a much smaller gradient in the slow direction compared to the fast direction. We note that the ray-tracing methods used here cannot test the feasibility of a small negative gradient for the slow direction, although this is not ruled out by the data. The inclusion of gradients in the inversion of the NoMelt data decorrelates the residuals with offset (Figure 7), although the effect is small. The interpretation of the inverted anisotropy is different for the model parameterizations with and without gradients. In the no-gradient models (Figures 5a–5c), the inverted anisotropy is averaged over the depth range that the *Pn* phase traveled. For the gradient parameterization (Figure 5d), the percent anisotropy applies to the very top of the mantle, and the value is smaller than the no-gradient cases in Figures 5 and 8, below. Our preferred gradient model implies an increase in anisotropy with depth.

3.6. Inversion Sensitivity Tests

The accuracy of the inversion method was tested using synthetic travel times. The synthetic data were generated by raytracing a set of offsets and azimuths through a prescribed anisotropic velocity model and adding 10 ms of random normal error. Synthetic data sets were first generated for a perfectly even distribution of offsets and azimuths. Iterative inversion of the synthetics recovered the percent anisotropy within 0.04%

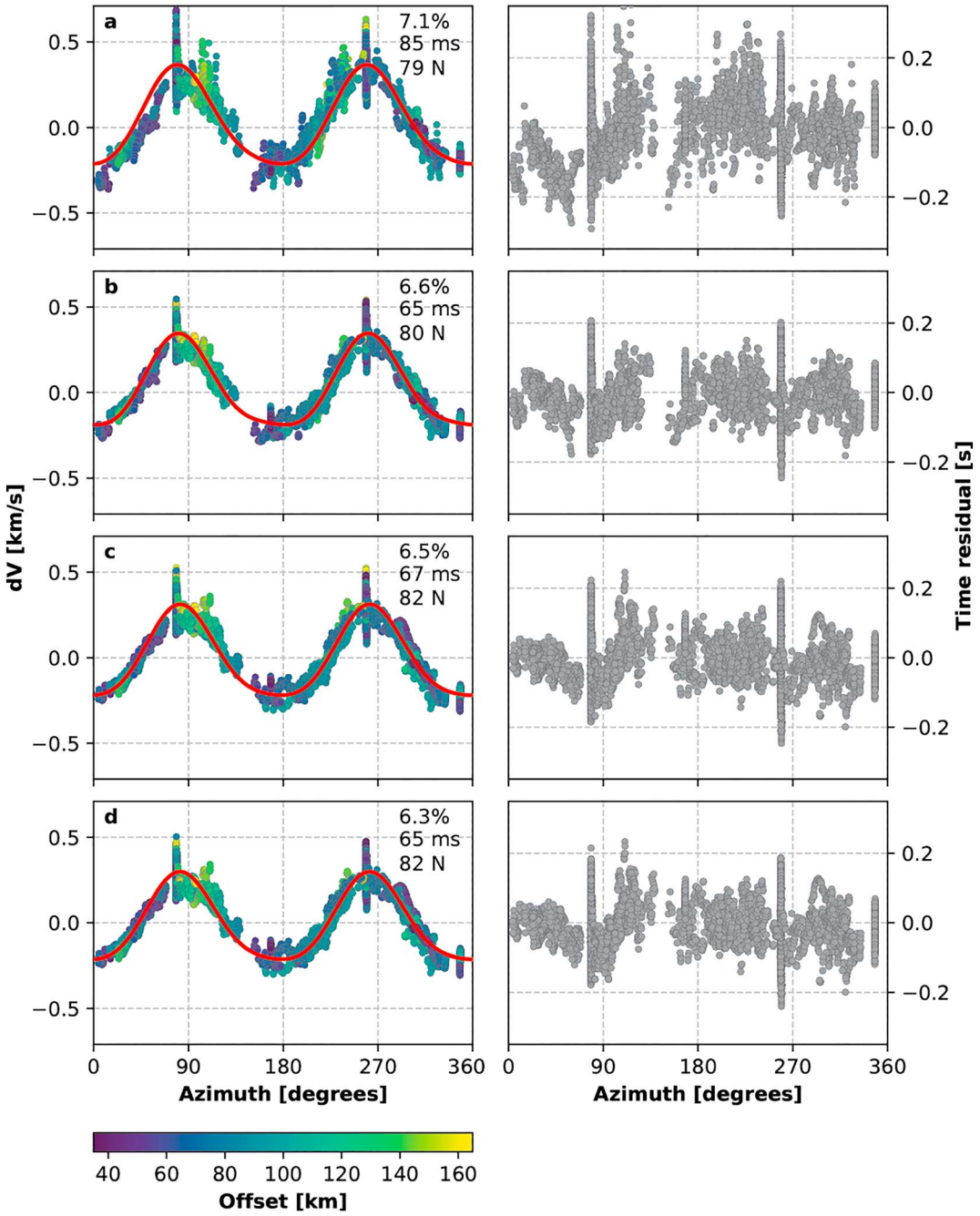

Figure 5. Inversion result (red line) and fitted data (left column; dots colored by source–receiver offset) with corresponding percent anisotropy, RMSE, and fast direction azimuth (top right corners), and residuals (right column). (a) Inversion with no statics, propagation correction using only the bin velocity model, and no gradients. (b) Same as in (a) but including static corrections. (c) With statics, 10 iterations on the propagation corrections, and no gradients. (d) With statics, 10 iterations, and the preferred gradient model. See text for discussion.

of the generating model, the isotropic velocity within 0.01 km/s, and the fast-direction azimuth within 0.07°N. To test the effects of the uneven data distribution, synthetic travel times were next generated with offsets and azimuths distributed as in the NoMelt data set. The unevenly distributed synthetic data did an equally good job of recovering all aspects of the generating model as the perfectly distributed synthetic data had. This indicates that there were sufficient data to avoid bias due to the distribution of offsets and azimuths assuming that the errors in the data are normally distributed.

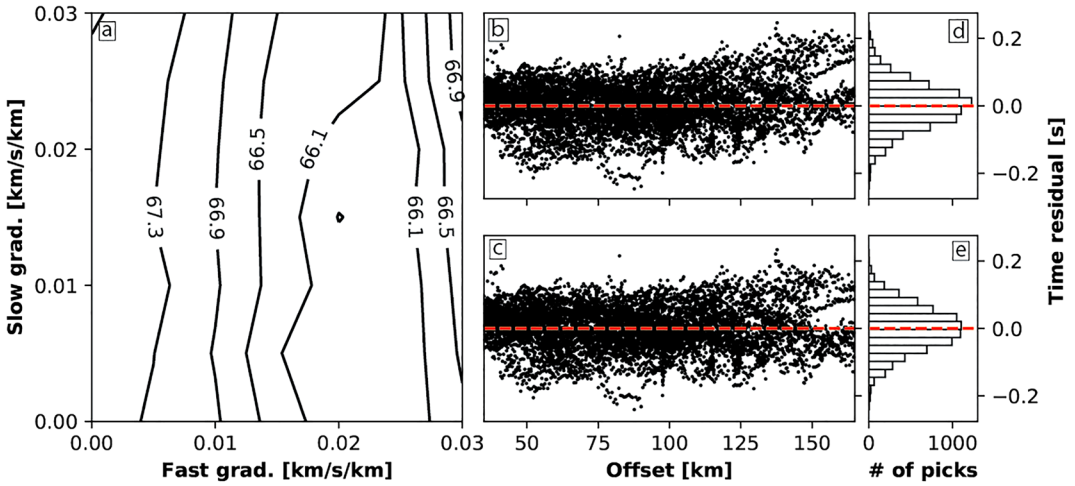

Figure 6. (a) Contours of RMSE in milliseconds for inversions of the NoMelt travel time data with different gradient models show a sensitivity to vertical velocity gradient, with greater sensitivity to the fast-direction gradient than the slow, similar to what is seen with the synthetic data in Figure 7. Our preferred model has a gradient of 0.02 km/s/km in the fast direction and 0 km/s/km in the slow direction. (b) Residuals from the model in Figure 5c, an inversion without gradients, show a slight correlation with offset, particularly for large offsets. (c) Residuals from the model in Figure 5d, inverted with the preferred gradient model, are flattened out at large offsets compared to (b). (d and e) Histograms show the distribution of time residuals for the two cases highlighted in (b) and (c).

While our inversion approach relies on isotropic ray tracing along particular azimuths to approximate travel times for an anisotropic medium, this is not expected to introduce significant errors into the calculations. Using isotropic ray tracing, as opposed to anisotropic ray tracing, is equivalent to assuming that the effect of transverse motion due to anisotropy is small, and previous studies have demonstrated that the effect is small for *P* wave travel times (Shearer & Orcutt, 1985).

Synthetic travel time data were also used to test how well the data could resolve gradients. Synthetics were generated using an anisotropic model with known velocity gradients and with the same azimuths and offsets as the real data set. The synthetic travel times were then inverted using the same method as the real data and the gradient values were grid-searched as described in section 3.5. The RMSE was higher and the residuals

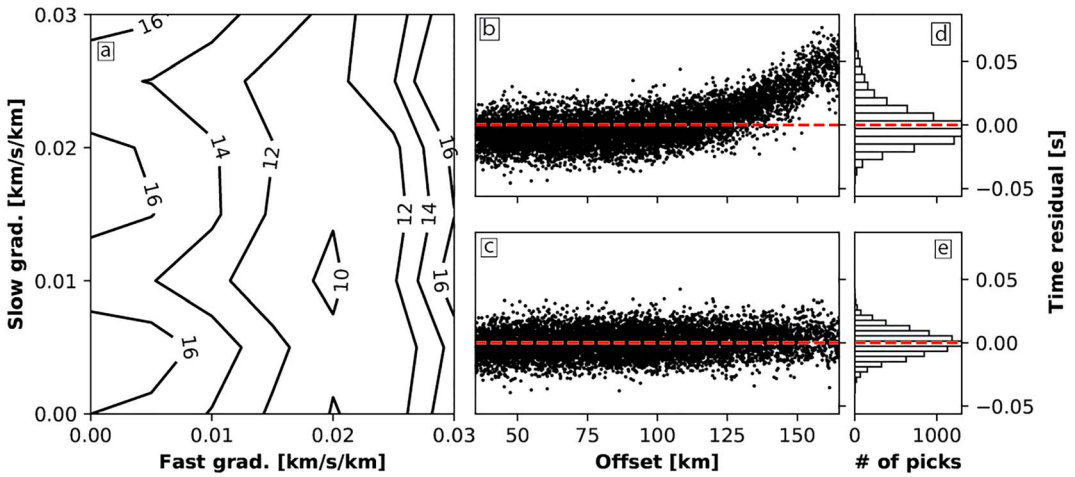

Figure 7. For synthetic data, generated using a velocity model with a 0.02-km/s/km gradient in the fast direction and 0 km/s/km in the slow direction. (a) Contours of RMSE for inversions with different gradient models (i.e., fast/slow pairs) show that the gradient model is well resolved in the fast direction, but is more ambiguous in the slow direction. (b) Inverting without gradients leads to a correlation of the residuals with offset. (c) When the same synthetic travel times are inverted with the true gradient model, the offset correlation disappears. (d and e) Histograms show the distribution of time residuals for the two gradient cases highlighted in (b) and (c).

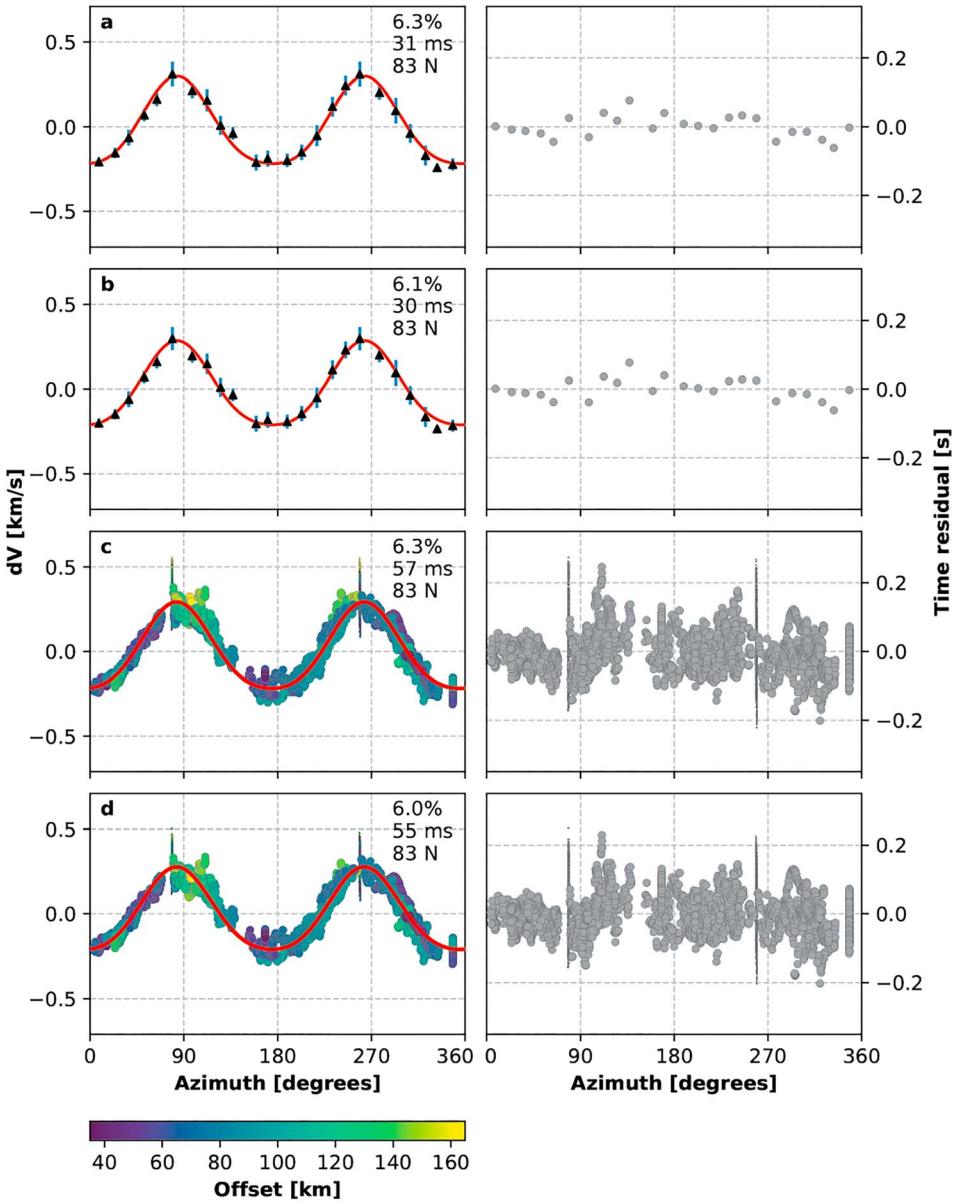

Figure 8. (a) Inversion results for the NoMelt travel time data with data averaged into 15° bins after the application of static and propagation corrections, including 10 iterations and no gradients. (b) Same as in (a) but with the preferred gradient model. (c) Inversion results for all of the NoMelt travel time data and using data weights in the inversion as described in the text. Weights are indicated by the size of plotted points. This model includes 10 iterations and no gradients. (d) Same as in (c) but with the preferred gradient model.

were strongly correlated with source–receiver offset for models where the gradients imposed in the inversion process differed from those used to generate the synthetics (Figure 7). The minimum RMSE for the synthetics corresponds to the correct gradient model, showing that RMSE can be used as an indicator for gradients, but the constraints on the slow direction gradient are much weaker than the constraints for the fast direction. This is likely because of the large range of offsets and large quantity of data available near the fast direction azimuth which is not matched for the slow direction.

While synthetic tests indicate that the distribution of data is sufficient to recover anisotropy parameters and constrain gradients in the case of normally distributed errors, the azimuthal patterns in the residuals illustrated in Figure 5 suggest that the data contain systematic errors. Such errors might arise if a swath of *Pn* arrivals has been picked systematically too early or late over successive shots, or if a broad region of the

crust or mantle violates our assumption of 1-D velocity structure. We tested for bias due to non-1-D structure by averaging the static- and propagation-corrected NoMelt data into 15° bins and inverting the bin averages with weights corresponding to the standard deviation of dV in each bin (Figures 8a and 8b). Since the data within a given bin come from a variety of OBS and have sampled the crust and mantle over different regions, this averaging tends to smooth out non-1-D effects and, if those effects are large, the weighting damps out their effect on the inversion. Binning also reduces the weight of the most populous bins along L02. The model obtained from the binned data is very similar to that obtained from the full inversion, with 6.3% anisotropy for the binned no-gradient parameterization versus 6.5% for the unbinned data, and 6.1% anisotropy for the binned gradient case versus 6.3% for the unbinned data. While the results of the binned fits suggest that lateral variations in crust or mantle velocity structure could be present, we believe that the influence of such features is small. Since the data near any given azimuth come from a variety of source–receiver pairs that will not generally have similar travel paths, systematic variations in crust or mantle structure should be averaged out in the 1-D model. Further, the travel time residuals do not show any coherent spatial trends indicative of systematic changes in crust or mantle structure across the portion of the NoMelt site considered in this study.

For both parameterizations, the fast direction in the binned data inversions is rotated 1° to 83°N relative to the 82°N fast direction found with the unbinned data. We tested whether this rotation was due primarily to sampling bias toward data from L02 azimuths by downweighting only the data along L02 azimuths in the inversion. Data weights were determined by the ratio of the median number of picks in non-L02 azimuthal bins to the numbers of picks along L02 azimuths. The weighting factors for L02 picks were on the order of 0.05, while non-L02 picks were given weights of 1. Inverting all of the data using this weighting scheme resulted in a fast direction along 83°N and slightly weaker anisotropy of 6.3% (Figure 8c) versus 6.5% (Figure 5c) for the unweighted inversion. This suggests that the sampling bias toward data along L02 azimuths does influence inversions using all of the travel time picks when weights are not applied, yielding a slightly higher percent anisotropy and a rotation of the fast direction 1° closer to the azimuth of L02. The mean velocity was the same in all inversions.

When a grid-search for gradient parameters is performed using the weighted inversion, the minimum RMSE is obtained with a larger fast-direction gradient of 0.027 km/s/km compared to 0.02 km/s/km when the data are not weighted. The RMSE minimum is also less well defined for the inversion of the weighted data than for the inversion of unweighted data, demonstrating that the data along L02 azimuths are the primary source of the constraint on the fast-direction gradient. This difference in the value of the preferred fast-direction gradient could be due to the relaxation of constraints provided by the deepest raypaths when the long-offset data along L02 are downweighted.

We also test for the influence of the 4θ terms of equation (2) on the inversion. All of the final models (Figures 5c, 5d, and 8a–8d) have nonzero coefficients for the 4θ terms, and these coefficients are an order of magnitude smaller than those of the 2θ terms (Table 1). We tested the influence of the 4θ terms on the inversion result by inverting the full, unweighted data set while holding each of the 4θ coefficients fixed. The results of a suite of such constrained inversions show that the 4θ terms have a significant effect on both the strength of anisotropy obtained in the inversion and the orientation of the fast direction (Figure 9). When both 4θ coefficients are set to zero and the travel time data are fit with only 2θ variation, the velocity in the slow direction drops and the strength of anisotropy increases from 6.3% to 6.8%, demonstrating that the 4θ terms are important to the overall fit of the NoMelt data even though the coefficients are small. Several previous studies fit only for 2θ coefficients because the 4θ terms are generally small. Our analysis suggests that such a choice leads to less accurate results. The 4θ terms are related to elastic parameters, and so setting them to zero imposes a constraint on the velocity structure of the medium that is not necessarily justified.

3.7. Final Model

The six models shown in Figures 5c, 5d, and 8a–8d all fit the travel time observations well. Models in Figures 5c, 8a, and 8c differ from Figures 5d, 8b, and 8d in their gradient parameterization. While the gradient parameterization used for Figures 5d, 8b, and 8d is more realistic and justifiable than the parameterization without gradients, models in Figures 5c, 8a, and 8c have value as simple and useful models that accurately characterize the average anisotropy of the upper several kilometers of a 1-D mantle. The models shown in Figure 5 use all of the individual travel times, whereas the models in Figures 8a and 8b are based on

Table 1
Parameters for Anisotropy and Elasticity Obtained in This Study

	Anisotropy Parameters		Elasticity Parameters (km/s)		Elasticity Parameters (GPa)	
All data, no gradients (Figure 5c)	Mean V_P (km/s)	8.14	A[a]	0.000	C_{11}	207.30
	Percent anisotropy	6.5%	B	−0.257	C_{22}	235.03
	Azimuth of maximum V_P (°N)	82/262	C	0.063	C_{16}	0.10
	Fast gradient (km/s/km)	0.0	D	0.038	C_{26}	3.29
	Slow gradient (km/s/km)	0.0	E	−0.028	$C_{12} + 2C_{66}$	212.57
All data, with gradients (Figure 5d)	Mean V_P (km/s)	8.14	A	0.000	C_{11}	207.29
	Percent anisotropy	6.3%	B	−0.247	C_{22}	233.94
	Azimuth of maximum V_P (°N)	82/262	C	0.060	C_{16}	0.07
	Fast gradient (km/s/km)	0.02	D	0.035	C_{26}	3.18
	Slow gradient (km/s/km)	0.0	E	−0.028	$C_{12} + 2C_{66}$	212.66
Binned data, no gradients (Figure 8a)	Mean V_P (km/s)	8.14	A	0.000	C_{11}	207.29
	Percent anisotropy	6.3%	B	−0.252	C_{22}	234.99
	Azimuth of maximum V_P (°N)	83/263	C	0.057	C_{16}	0.12
	Fast gradient (km/s/km)	0.0	D	0.035	C_{26}	3.30
	Slow gradient (km/s/km)	0.0	E	−0.020	$C_{12} + 2C_{66}$	212.60
Binned data, with gradients (Figure 8b)	Mean V_P (km/s)	8.14	A	0.000	C_{11}	207.27
	Percent anisotropy	6.1%	B	−0.242	C_{22}	233.88
	Azimuth of maximum V_P (°N)	83/263	C	0.054	C_{16}	0.08
	Fast gradient (km/s/km)	0.02	D	0.033	C_{26}	3.21
	Slow gradient (km/s/km)	0.0	E	−0.019	$C_{12} + 2C_{66}$	212.73
Weighted data, no gradients (Figure 8c)	Mean V_P (km/s)	8.14	A	0.000	C_{11}	207.18
	Percent anisotropy	6.3%	B	−0.248	C_{22}	233.90
	Azimuth of maximum V_P (°N)	83/263	C	0.058	C_{16}	0.53
	Fast gradient (km/s/km)	0.0	D	0.032	C_{26}	2.61
	Slow gradient (km/s/km)	0.0	E	−0.018	$C_{12} + 2C_{66}$	213.22
Weighted data, with gradients (Figure 8d)	Mean V_P (km/s)	8.13	A	0.000	C_{11}	207.15
	Percent anisotropy	6.0%	B	−0.238	C_{22}	232.71
	Azimuth of maximum V_P (°N)	83/263	C	0.056	C_{16}	0.53
	Fast gradient (km/s/km)	0.02	D	0.029	C_{26}	2.47
	Slow gradient (km/s/km)	0.0	E	−0.017	$C_{12} + 2C_{66}$	213.39

[a]Coefficients A, B, C, D, and E correspond to equation (4).

averages of data within 15° bins, and those in Figures 8c and 8d are based on weighted data with points along L02 azimuths downweighted relative to the rest of the data. The models based on bin averages smooth out effects related to systematic data errors, while the models based on all of the data individually may be a more accurate representation of the Earth, despite some systematic misfits to the data indicated by trends in the residuals. The same fast-direction azimuth is obtained for all the models in Figure 8, suggesting that downweighting data along L02 effectively mitigates bias in the fast direction estimate without requiring full binning of the data.

Our preferred model is shown in Figure 8d. It is a fit to data that have been corrected in a self-consistent manner, and it includes a parameterization of vertical velocity gradients that we believe is more realistic than a mantle with zero vertical velocity gradients. The inclusion of gradients reduces the RMSE of the model relative to the parameterization without gradients, and also decorrelates the residuals with offset. This anisotropy model is based on the inversion of weighted data, with points along L02 azimuths downweighted to minimize the biasing effects of data along L02, combined with gradients determined by inversion of the full data set. The gradient model therefore makes use of the information provided by data along L02 to better constrain the fast-direction gradient. This model has 6.0% azimuthal anisotropy in *P* wave velocities at the Moho, with a mean velocity of 8.13 km/s, a fast-direction vertical velocity gradient of

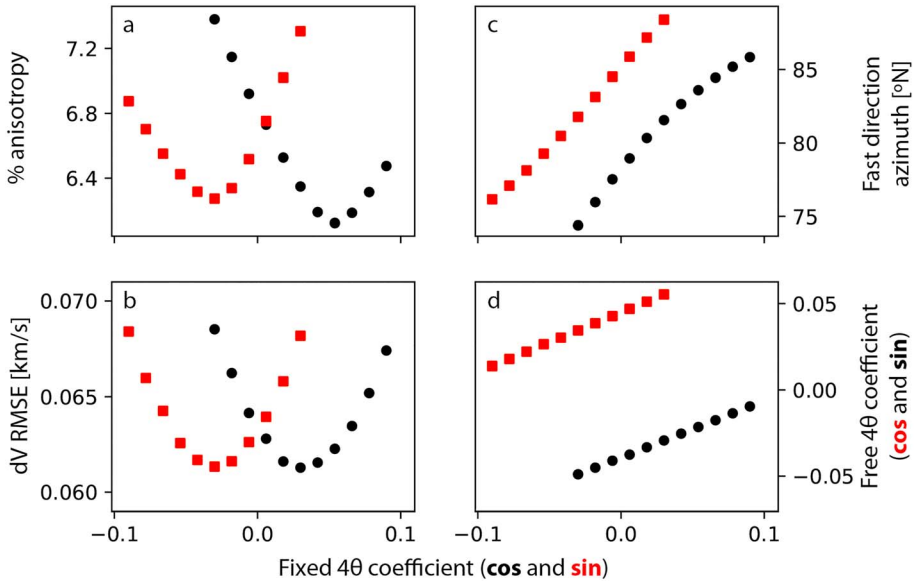

Figure 9. Velocity models were fit with each of the two 4θ coefficients held constant at different values. Panels show the value of the fixed cosine (black circles) and sine (red squares) 4θ coefficients versus (a) percent anisotropy, (b) RMSE of the velocity variation dV, (c) fast-direction azimuth, and (d) value for the free 4θ coefficient.

0.02 km/s/km, and a slow-direction gradient of 0 km/s/km. The fast-direction azimuth of 83°/263°N is normal to magnetic anomalies (Barckhausen et al., 2013). Based on the range of models obtained by the different weighting and binning schemes, and on our tests with synthetic data, we estimate the uncertainty in the strength of anisotropy to be ±0.3% and the uncertainty in the fast-direction azimuth to be ±1°. The travel time predictions from this model are in good agreement with the data (Figure 10).

The detailed characteristics of our preferred model and the five other models are provided in Table 1. These characteristics include calculated elements of the elastic tensor. For small azimuthal anisotropy, the square of the P wave velocity can be approximated by the same function form as the velocity variations:

$$V^2(\theta) \approx \widehat{A} + \widehat{B}\cos 2\theta + \widehat{C}\sin 2\theta + \widehat{D}\cos 4\theta + \widehat{E}\sin 4\theta \quad (7)$$

where $\widehat{A}, \widehat{B}, \widehat{C}, \widehat{D}$, and $\widehat{E}$ are linear functions of the elastic parameters of the material (Backus, 1965; Crampin, 1984). The squared velocities of the final models were inverted to obtain $\widehat{A}, \widehat{B}, \widehat{C}, \widehat{D}$, and $\widehat{E}$ coefficients. These coefficients uniquely determine four of the elastic parameters and place a constraint on two others (Table 1).

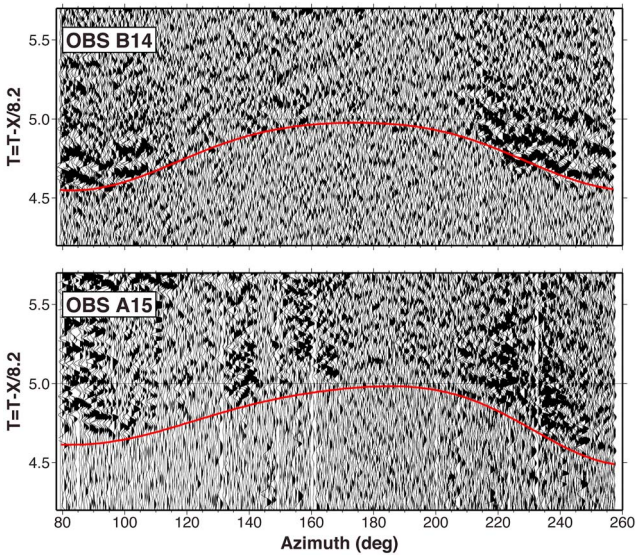

Figure 10. L04 data from OBS B14 and A15 show good agreement between *Pn* first arrivals and arrival times predicted by our preferred anisotropic velocity model (red lines).

4. Discussion

Our measurement of azimuthal anisotropy and vertical velocity gradients in 70-Ma oceanic lithosphere at the NoMelt site provides estimates of the fast-direction orientation, strength, and depth gradients of anisotropy in the upper ~7 km of the oceanic mantle. These quantities reflect the dynamics of mantle deformation during lithospheric formation as well as processes involved in lithospheric evolution as the plate aged. The anisotropic structure at the NoMelt site is consistent with a simple model of mineral fabric formed by 2-D corner flow and subsequent plate-driven shear at a mid-ocean ridge combined with some mechanism, such as the decreasing density of oriented cracks or joints with depth, that imparts an azimuthal variation in vertical velocity gradient. The NoMelt site was chosen owing to its uncomplicated tectonic history, and the mantle

structure at this location is presumably indicative of a correspondingly uncomplicated mode of lithospheric formation at intermediate spreading rates. The NoMelt results thus provide a reference structure for comparison with results from lithosphere formed at different spreading rates or in more complex settings, where differences in anisotropic structure can then be interpreted to reflect differences in mantle dynamics.

4.1. Fast Direction Orientation

The fast direction of anisotropy from seismic studies is typically interpreted as representing a strong concentration of olivine *a* axes aligned by shear to parallel the azimuth of the major axis of the finite strain ellipse (e.g., Hess, 1964; Nicolas & Christensen, 1987). While the orientation of the fast direction can also be affected by deformation history (e.g., Boneh et al., 2015; Boneh & Skemer, 2014), mineralogy (e.g., Mainprice, Barruol & Ismaïl 2000), water content (e.g., Jung & Karato, 2001), melt (e.g., Holtzman et al., 2003), and other factors, broad agreement between models and observations for regions like the central Pacific (e.g., Becker et al., 2014) suggests that the fast direction at the NoMelt site can be interpreted in terms of strain associated with plate spreading. At the NoMelt site, we find the fast direction of anisotropy directed along 83/263°N, consistent with the presence of A-type olivine fabric formed by 2-D mantle flow. The paleospreading direction at the center of the NoMelt array is estimated to be along 82°N based on local magnetic anomalies striking at 172°N (Barckhausen et al., 2013). We estimate an approximately 1° uncertainty in the fast-direction azimuth based on the range of fast azimuths from the six final models. Thus, within uncertainty, the measured fast azimuth coincides with the local paleospreading direction. This result suggests that this section of oceanic lithosphere experienced predominantly 2-D mantle flow during its formation at the ridge.

The alignment of the fast and paleospreading directions at the NoMelt site is not particularly surprising; the NoMelt site was purposely located in the center of a wide, stable spreading segment where the lithosphere was likely to have experienced primarily 2-D mantle flow. However, other active-source observations do not strongly support the expectation that fast and paleospreading directions are aligned. Many previous refraction-derived anisotropy measurements have found fast directions rotated several degrees away from the paleospreading direction, including a rotation of 13° near Hawaii (Morris et al., 1969), 17° near 45°N along the Mid-Atlantic Ridge (Keen & Tramontini, 1970), 17° off the coast of British Columbia (Keen & Barrett, 1971), 27° in the southwest Pacific (Shearer & Orcutt, 1985), and 15° in the western Pacific (Shintaku et al., 2014). In several studies, anisotropy initially characterized as spreading-parallel has later been recognized as skewed based on improved estimates of paleospreading directions (e.g., Morris et al., 1969; Shearer & Orcutt, 1985). While some of these previous studies suffer from poor data quality and/or lack of azimuthal coverage, the predominance in the literature of observations where the paleospreading and fast directions do not align suggests that mantle flow patterns at mid-ocean ridges may commonly be more complex than 2-D corner flow, perhaps involving contributions from dynamic flow in the asthenosphere that influence the formation of lithospheric fabric. For anisotropy measurements based on *Pn* travel times along a section of the East Pacific Rise near 9°N, the fast direction is rotated ~10° with respect to plate spreading (Toomey et al., 2007), and anisotropy measurements based on *Pn* phases and SKS splits around the Juan de Fuca ridge show a fast direction rotated by ~18° relative to the paleospreading direction (VanderBeek et al., 2016; VanderBeek & Toomey, 2017). These studies lead to speculation that this angular divergence represents a skewness between absolute plate motion (APM) and the plate-spreading direction. This could reflect a lag between changing asthenospheric flow and the plate-kinematic response, which may require changes in ridge segmentation (Toomey et al., 2007).

Plate reconstruction models (Seton et al., 2012) suggest that APM and paleospreading directions were not coincident when and where the NoMelt site was formed. However, our results suggest that deformation at this intermediate-rate ridge was dominated by 2-D mantle flow associated with relative plate motion. Surface wave constraints on asthenospheric anisotropy at the NoMelt site also do not see a fast direction aligned with APM within the upper 300 km of the mantle (Lin et al., 2016). This has been interpreted as indicating that on a regional scale, spreading-derived CPO and dynamic flow in the asthenosphere dominate over fabric related to APM. The NoMelt results are consistent with estimates of fast direction orientation based on global surface wave tomography, which show close alignment of the fast and paleospreading directions for most Pacific lithosphere younger than 70 Ma (e.g., Becker et al., 2014). The surface wave results of Becker et al. (2014) do show large systematic differences in many other locations, including most of the Atlantic. The effects of non-2-D mantle flow and other factors, such as melt supply and spreading rate, on

lithospheric fabric could be evaluated in more detail by further comparisons of absolute plate motion and paleospreading directions using refraction-based measurements of anisotropy at particular locations.

4.2. Depth Variation of Anisotropy

The estimate of azimuthally varying vertical velocity gradients at the NoMelt site implies a depth variation in anisotropy. This depth variation could represent changes in intrinsic anisotropy related to mineral fabric, extrinsic anisotropy related to cracks or other aligned structures, or some combination of both. The gradient estimate is pinned to a parameterization motivated by the observation that *Pn* amplitudes tend to decrease at azimuths away from the fast direction (Figures 3 and 10). However, the gradient estimate under this parameterization is based solely on travel time misfit. Our efforts to include quantitative information on *Pn* amplitudes in the gradient estimation were complicated by the focusing and defocusing effects of seafloor structure which dominate the amplitude signal. Nevertheless, the basic observation of nonzero *Pn* amplitudes at all azimuths places some constraints on the mechanisms producing the estimated depth variation in anisotropy.

The most common interpretation of anisotropy in the uppermost oceanic mantle is as intrinsic anisotropy resulting from CPO of olivine imparted by shear strain. An interpretation of anisotropy solely in terms of CPO implies that the increase in the strength of anisotropy with depth corresponds to an increase in fabric strength with depth. Numerical models of corner flow do predict an increase in the strength of anisotropic fabric with depth in the shallow mantle (Blackman et al., 1996, 2017; Blackman & Kendall, 2002), but these models focus on asthenospheric anisotropy and do not resolve the details of fabric in the lithosphere.

While an increase in fabric strength is one possibility, azimuthal variation in vertical velocity gradients could also come from other sources. For example, fabrics other than olivine CPO may develop at mid-ocean ridges and impart intrinsic anisotropy. In particular, deformation experiments conducted on olivine aggregates with melt present (e.g., Hansen et al., 2016, 4% melt; Qi et al., 2018, 7% melt) produce fabrics that appear to be a combination of CPO and shape-preferred orientation (Hansen et al., 2014, 2016; Holtzman et al., 2003; Qi et al., 2018). At the much lower melt fractions typical of mid-ocean ridges, anisotropy due to this melt-present fabric is still likely to be dominated by the CPO component aligned in the shear direction, but the strength of effective seismic anisotropy may be reduced (Hansen et al., 2016; Zhong et al., 2014). It is possible that this mechanism would impart vertical gradients in anisotropy if the percentage of melt present along a corner-flow flow line decreased for progressively deeper flow lines.

Extrinsic mechanisms such as cracks, joints, and vertical layering could also produce the observed change in anisotropy with depth. The closure of microcracks with increasing depth and pressure or, equivalently, a decrease in the occurrence of cracks with depth (e.g., Demartin et al., 2004), could reasonably produce the observed positive vertical velocity gradients in the fast direction. Microcracks, if present, are expected to close within the depth range sampled in this study. The strength of anisotropy in our final model increases to ~7.7% at 7 km below the Moho, the maximum depth sampled by our data (Figure 11); this is close to the average *P* wave anisotropy estimated from olivine fabrics of ophiolite samples (8%), a value that does not include any effects from cracks (Ben Ismaïl & Mainprice, 1998). Laboratory measurements demonstrate crack closure pressures in dunite samples ranging from 250 to 750 MPa (Birch, 1960; Christensen, 1974; Greenfield & Graham, 1996), with most measurements below 400 MPa. Subtracting a hydrostatic pressure gradient from a lithostatic pressure gradient, we estimate an effective pressure of ~110 MPa at the Moho and ~265 MPa at 7 km below the Moho. This is within the range of experimentally determined crack closure pressures. The velocity gradient in the fast direction of the final model lies within the range of measurements of V_p with pressure made on dunite samples compiled by Greenfield and Graham (1996) (Figure 11).

While the magnitude of the fast-direction gradient can be explained by the closure of randomly oriented microcracks, explaining the azimuthal variation of the velocity gradient with crack closure requires oriented cracks, which are expected to produce azimuthally varying velocities (e.g., D. L. Anderson et al., 1974; Nishizawa, 1982). Thin, water-filled, oriented cracks cannot explain the observations, since they introduce a 4θ variation in velocity (e.g., Hudson, 1981), and the 4θ terms in all of our models are small (Table 1). The observed gradients can be explained by "dry" oriented microcracks filled with damaged material and/or hydrous alteration products, which are predicted to produce a 2θ velocity signal (Hudson, 1981; Thomsen, 1995). Assuming that the velocity at 7-km depth is representative of the uncracked solid, the

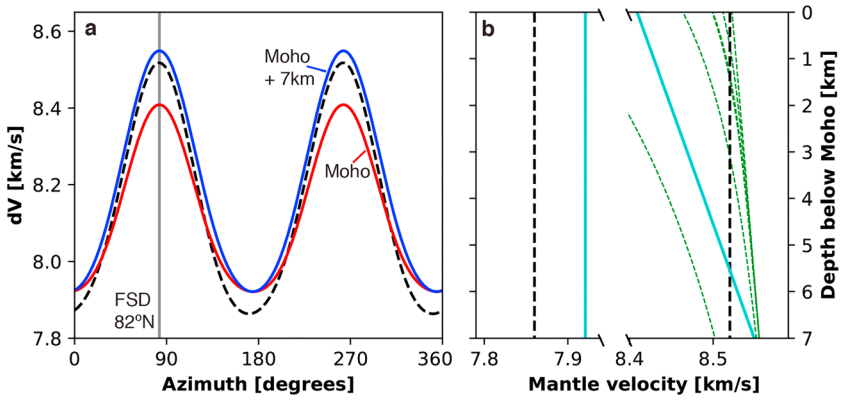

Figure 11. (a) The final model is shown at the Moho (red line) and 7 km below the Moho (blue line). An average model from ophiolite fabrics is shown for comparison (dashed black line; Ben Ismaïl & Mainprice, 1998). The fossil spreading direction, 82°N, is marked by a gray line. (b) The velocities in the fast and slow directions are shown versus depth below the Moho for the final model (cyan) and an average ophiolite model (dashed black). Dotted green lines show predicted velocity variation due to crack closure in dunite samples based on experimentally measured parameters compiled in Table 4 of Greenfield and Graham (1996) and calculated using equation (2) of that paper.

velocity at the Moho in the fast direction can be accounted for with a dimensionless crack density of ~0.05 (e.g., Crampin et al., 1980; Garbin & Knopoff, 1973, 1975a, 1975b) where the crack density is defined as $\varepsilon = Na^3/v$ for N cracks of radius a in a volume v. Since cracks filled with hydrous minerals would not be expected to close, the crack density for filled cracks would need to decrease with depth. Under the assumption that the entire volume of the cracks is serpentinized, a crack density of 0.05 corresponds to ~0.5 wt% water in the uppermost few kilometers of the mantle (Carlson & Miller, 2003). The oriented cracks would need to be aligned perpendicular to the paleospreading direction. This alignment would be consistent with the stress field experienced by the lithosphere near the ridge (Dunn, 2015), but horizontal extensional stress due to thermal contraction may be at a maximum normal to the plate spreading direction at older ages (e.g., Sandwell & Fialko, 2004; Sasajima & Ito, 2017). Joints and other types of layering, such as spatial variation in the density of microcracks or gabbroic dikes (e.g., Francheteau et al., 1990; Hekinian et al., 1993), can also produce an extrinsic transverse isotropy for the wavelengths typical of active-source seismic experiments (e.g., Backus, 1962). Cracks or melt bodies localized into ridge-parallel structures could conceivably be generated by time-varying magmatism and thermal structure at a mid-ocean ridge.

While various kinds of extrinsic anisotropy may be present, they all involve important unknowns. Of the interpretations suggested here, the combination of corner flow and aligned microcracks seems the most plausible to us given what is known. Regardless of the mechanism, however, a key point to be noted from the gradient measurement is that the strength of anisotropy at 7 km below the Moho in the preferred model is estimated to be significantly higher than the depth-averaged strength of anisotropy estimated from the same data without the gradient parameterization. This suggests that information is being lost when anisotropy is inverted for using binned data, and that the maximum strength of anisotropy in the lithospheric mantle may be underestimated by studies where vertical gradients are not accounted for.

4.3. Using Measurements of Upper Mantle Anisotropy

Measurements of seismic anisotropy provide a means to learn about oceanic plate formation and mantle flow. This is possible because the evolution of lithospheric anisotropy is sensitive to a variety of factors including preexisting mantle fabric (Boneh & Skemer, 2014; Skemer et al., 2012), the amount of strain the lithosphere experiences (e.g., Hedjazian & Kaminski, 2014; Ribe, 1992; Zhang & Karato, 1995), the magnitude of shear strain relative to the rate of rotation of the strain axes (Kaminski & Ribe, 2002), and the presence of melt during deformation (Hansen et al., 2016; Qi et al., 2018). At the same time, this variety of sensitivities can make the interpretation of anisotropy difficult. Active source measurements of oceanic uppermost mantle seismic anisotropy to date have provided estimates of fast-direction orientation and the strength of anisotropy, giving strong support for mantle flow accompanying plate separation at mid-ocean ridges. However, these results have not placed strong constraints on most of the factors that affect fabric

development, so many predictions that relate anisotropy to dynamic mid-ocean ridge processes (e.g., Blackman et al., 1996; Blackman & Kendall, 2002) remain untested.

The NoMelt results show that the addition of a constraint on the depth variation of anisotropy forces a consideration of multiple factors that impart seismic anisotropy, demonstrating a sensitivity to at least some of those factors. While our interpretation of these results is speculative, the sensitivity of the observations suggests a path forward. Differences in anisotropy, measured in a standard way, between oceanic lithosphere formed under different conditions can be used to infer variations in plate formation processes. Further, anisotropy measurements made at different ages within an otherwise relatively homogeneous segment can be used to understand how a plate evolves as it ages and, in particular, how the lithosphere responds to thermal contraction. Results from the NoMelt site provide a useful reference for this type of comparative study.

5. Conclusions

We have measured 6.0 ± 0.3% anisotropy at the Moho and azimuthally varying vertical velocity gradients in the upper 7 km of the mantle at the NoMelt site in the central Pacific. The fast direction is oriented parallel to paleospreading within an uncertainty of ±1°, consistent with predictions for olivine fabric formed by 2-D mid-ocean ridge corner flow. Our preferred gradient model, which varies azimuthally between 0.02 km/s/km in the fast direction and 0 km/s/km in the slow direction, implies that effective anisotropy increases with depth, reaching a value of 7.7% at 7 km below the Moho. We interpret the increase in anisotropy with depth as reflecting the diminishing influence of an extrinsic anisotropy that is orthogonal to the intrinsic anisotropy, as opposed to intrinsic anisotropy increasing as a function of depth. The extrinsic anisotropy can be explained by some form of organized or aligned cracks closing or otherwise decreasing in density with depth.

This study demonstrates the value of comprehensive azimuthal coverage, controls on shallow structure, and long source–receiver offsets for measuring anisotropy with depth constraints. The constraint on vertical velocity gradients enables us to consider multiple factors that affect the formation and evolution of the lithospheric mantle. Constraints on shallow structure are key to estimating gradients, as deterministic static corrections based on NoMelt MCS and swath bathymetry data provide a reduction in residuals that is on the order of the delay-time signal of anisotropy. This measurement of anisotropy in 70-Myr-old lithosphere formed at an intermediate-to-fast spreading rate can serve as a reference for comparative studies of lithospheric formation and evolution.

Acknowledgments
We thank the Captain and crew of the R/V *Marcus G. Langseth* and the engineers and technicians from the Scripps Institution of Oceanography and the Woods Hole Oceanographic Institution, who provided the instruments through the National Science Foundation's Ocean Bottom Seismograph Instrument Pool (OBSIP). The professionalism and expertise of these individuals were key to the success of this experiment. We also thank Donna Blackman, Tom Brocher, Philip Skemer, and an anonymous reviewer for their thoughtful comments which greatly improved this paper. The OBS data described here are archived at the IRIS Data Management Center (http://www.iris.edu) under network code ZA 2011–2013. The travel time picks are archived in the Marine-Geo Digital Library (http://www.marine-geo.org/library/) with the DOI 10.1594/IEDA/324643. This work was supported by NSF grant OCE-0928663 to D. Lizarralde, J. Collins, and R. Evans; NSF grant OCE-0927172 to G. Hirth; NSF grant OCE-0928270 to J. Gaherty; and an NSF Graduate Research Fellowship to H. Mark.

References

Anderson, D. L., Minster, B., & Cole, D. (1974). The effect of oriented cracks on seismic velocities. *Journal of Geophysical Research*, *79*(26), 4011–4015. https://doi.org/10.1029/JB079i026p04011

Anderson, O. L., Schreiber, E., Liebermann, R. C., & Soga, N. (1968). Some elastic constant data on minerals relevant to geophysics. *Reviews of Geophysics*, *6*(4), 491–524. https://doi.org/10.1029/RG006i004p00491

Backus, G. E. (1962). Long-wave elastic anisotropy produced by horizontal layering. *Journal of Geophysical Research*, *67*(11), 4427–4440. https://doi.org/10.1029/JZ067i011p04427

Backus, G. E. (1965). Possible forms of seismic anisotropy of the uppermost mantle under oceans. *Journal of Geophysical Research*, *70*(14), 3429–3439. https://doi.org/10.1029/JZ070i014p03429

Barckhausen, U., Bagge, M., & Wilson, D. S. (2013). Seafloor spreading anomalies and crustal ages of the Clarion-Clipperton Zone. *Marine Geophysical Research*, *34*(2), 79–88. https://doi.org/10.1007/s11001-013-9184-6

Becker, T. W., Conrad, C. P., Schaeffer, A. J., & Lebedev, S. (2014). Origin of azimuthal seismic anisotropy in oceanic plates and mantle. *Earth and Planetary Science Letters*, *401*, 236–250. https://doi.org/10.1016/j.epsl.2014.06.014

Ben Ismaïl, W., & Mainprice, D. (1998). An olivine fabric database: An overview of upper mantle fabrics and seismic anisotropy. *Tectonophysics*, *296*(1-2), 145–157. https://doi.org/10.1016/S0040-1951(98)00141-3

Birch, F. (1960). The velocity of compressional waves in rocks to 10 kilobars, part 1. *Journal of Geophysical Research*, *65*(4), 1083–1102. https://doi.org/10.1029/JZ065i004p01083

Blackman, D. K., Boyce, D. E., Castelnau, O., Dawson, P. R., & Laske, G. (2017). Effects of crystal preferred orientation on upper mantle flow near plate boundaries: Rheologic feedbacks and seismic anisotropy. *Geophysical Journal International.*, *210*(3), 1481–1493. https://doi.org/10.1093/gji/ggx251

Blackman, D. K., & Kendall, J.-M. (2002). Seismic anisotropy in the upper mantle 2. Predictions for current plate boundary flow models. *Geochemistry, Geophysics, Geosystems*, *3*(9), 8602. https://doi.org/10.1029/2001GC000247

Blackman, D. K., Kendall, J.-M., Dawson, P. R., Wenk, H.-R., Boyce, D., & Morgan, J. P. (1996). Teleseismic imaging of subaxial flow at mid-ocean ridges: Traveltime effects of anisotropic mineral texture in the mantle. *Geophysical Journal International*, *127*(2), 415–426. https://doi.org/10.1111/j.1365-246X.1996.tb04730.x

Boneh, Y., Morales, L. F. G., Kaminski, E., & Skemer, P. (2015). Modeling olivine CPO evolution with complex deformation histories: Implications for the interpretation of seismic anisotropy in the mantle. *Geochemistry, Geophysics, Geosystems*, *16*, 3436–3455. https://doi.org/10.1002/2015GC005964

Boneh, Y., & Skemer, P. (2014). The effect of deformation history on the evolution of olivine CPO. *Earth and Planetary Science Letters*, *406*, 213–222. https://doi.org/10.1016/j.epsl.2014.09.018

Bratt, S. R., & Purdy, G. M. (1984). Structure and variability of oceanic crust on the flanks of the East Pacific rise between 11° and 13°N. *Journal of Geophysical Research*, *89*(B7), 6111–6125. https://doi.org/10.1029/JB089iB07p06111

Carlson, R. L., & Miller, D. J. (2003). Mantle wedge water contents estimated from seismic velocities in partially serpentinized peridotites. *Geophysical Research Letters*, *30*(5), 1250. https://doi.org/10.1029/2002GL016600

Christensen, N. I. (1974). Compressional wave velocities in possible mantle rocks to pressures of 30 kilobars. *Journal of Geophysical Research*, *79*(2), 407–412. https://doi.org/10.1029/JB079i002p00407

Christensen, N. I. (1979). Compressional wave velocities in rocks at high temperatures and pressures, critical thermal gradients, and crustal low-velocity zones. *Journal of Geophysical Research*, *84*(B12), 6849–6857. https://doi.org/10.1029/JB084iB12p06849

Constantin, M., Hékinian, R., Ackermand, D., & Stoffers, P. (1995). Mafic and ultramafic intrusions into upper mantle peridotites from fast spreading centers of the Easter microplate (south East Pacific). In *Mantle and Lower Crust Exposed in Oceanic Ridges and in Ophiolites* (pp. 71–120). Dordrecht: Springer. https://doi.org/10.1007/978-94-015-8585-9_4

Cormier, M.-H., Gans, K. D., & Wilson, D. S. (2011). Gravity lineaments of the Cocos plate: Evidence for a thermal contraction crack origin. *Geochemistry, Geophysics, Geosystems*, *12*, Q07007. https://doi.org/10.1029/2011GC003573

Crampin, S. (1984). An introduction to wave propagation in anisotropic media. *Geophysical Journal International*, *76*(1), 17–28. https://doi.org/10.1111/j.1365-246X.1984.tb05018.x

Crampin, S., McGonigle, R., & Bamford, D. (1980). Estimating crack parameters from observations of *P*-wave velocity anisotropy. *Geophysics*, *45*(3), 345–360. https://doi.org/10.1190/1.1441086

Demartin, B., Hirth, G., & Evans, B. (2004). Experimental constraints on thermal cracking of peridotite at oceanic spreading centers. In *Mid-Ocean Ridges* (pp. 167–185). Washington, DC: American Geophysical Union. https://doi.org/10.1029/148GM07

Dick, H. J., Fisher, R. L., & Bryan, W. B. (1984). Mineralogic variability of the uppermost mantle along mid-ocean ridges. *Earth and Planetary Science Letters*, *69*(1), 88–106. https://doi.org/10.1016/0012-821X(84)90076-1

Dunn, R. A. (2015). Tracking stress and hydrothermal activity along the eastern Lau spreading center using seismic anisotropy. *Earth and Planetary Science Letters*, *410*, 105–116. https://doi.org/10.1016/j.epsl.2014.11.027

Dunn, R. A., & Toomey, D. R. (1997). Seismological evidence for three-dimensional melt migration beneath the East Pacific rise. *Nature*, *388*(6639), 259–262. https://doi.org/10.1038/40831

Fowler, C. M. R. (2005). *The Solid Earth: An Introduction to Global Geophysics*. Cambridge University Press.

Francheteau, J., Armijo, R., Cheminée, J. L., Hekinian, R., Lonsdale, P., & Blum, N. (1990). 1 Ma East Pacific rise oceanic crust and uppermost mantle exposed by rifting in Hess deep (equatorial Pacific Ocean). *Earth and Planetary Science Letters*, *101*(2–4), 281–295. https://doi.org/10.1016/0012-821X(90)90160-Y

Gaherty, J. B., Lizarralde, D., Collins, J. A., Hirth, G., & Kim, S. (2004). Mantle deformation during slow seafloor spreading constrained by observations of seismic anisotropy in the western Atlantic. *Earth and Planetary Science Letters*, *228*(3–4), 255–265. https://doi.org/10.1016/j.epsl.2004.10.026

Garbin, H. D., & Knopoff, L. (1973). The compressional modulus of a material permeated by a random distribution of circular cracks. *Quarterly of Applied Mathematics*, *30*(4), 453–464. https://doi.org/10.1090/qam/99719

Garbin, H. D., & Knopoff, L. (1975a). Elastic moduli of a medium with liquid-filled cracks. *Quarterly of Applied Mathematics*, *33*(3), 301–303. https://doi.org/10.1090/qam/99661

Garbin, H. D., & Knopoff, L. (1975b). The shear modulus of a material permeated by a random distribution of free circular cracks. *Quarterly of Applied Mathematics*, *33*(3), 296–300. https://doi.org/10.1090/qam/99662

Garmany, J. (1981). Anisotropic gradients in the upper mantle. *Geophysical Research Letters*, *8*(9), 955–957. https://doi.org/10.1029/GL008i009p00955

Greenfield, R. J., & Graham, E. K. (1996). Application of a simple relation for describing wave velocity as a function of pressure in rocks containing microcracks. *Journal of Geophysical Research*, *101*(B3), 5643–5652. https://doi.org/10.1029/95JB03462

Hansen, L. N., Qi, C., & Warren, J. M. (2016). Olivine anisotropy suggests Gutenberg discontinuity is not the base of the lithosphere. *Proceedings of the National Academy of Sciences*, *113*(38), 10503–10506. https://doi.org/10.1073/pnas.1608269113

Hansen, L. N., Zhao, Y.-H., Zimmerman, M. E., & Kohlstedt, D. L. (2014). Protracted fabric evolution in olivine: Implications for the relationship among strain, crystallographic fabric, and seismic anisotropy. *Earth and Planetary Science Letters*, *387*, 157–168. https://doi.org/10.1016/j.epsl.2013.11.009

Hedjazian, N., & Kaminski, E. (2014). Defining a proxy for the interpretation of seismic anisotropy in non-Newtonian mantle flows. *Geophysical Research Letters*, *41*, 7065–7072. https://doi.org/10.1002/2014GL061372

Hekinian, R., Bideau, D., Francheteau, J., Cheminee, J. L., Armijo, R., Lonsdale, P., & Blum, N. (1993). Petrology of the East Pacific rise crust and upper mantle exposed in Hess deep (eastern equatorial Pacific). *Journal of Geophysical Research*, *98*(B5), 8069–8094. https://doi.org/10.1029/92JB02072

Henkart, P. (2003). Seismic processing system SIOSEIS. Retrieved March 20, 2017, from http://sioseis.ucsd.edu/

Hess, H. H. (1964). Seismic anisotropy of the uppermost mantle under oceans. *Nature*, *203*(4945), 629–631. https://doi.org/10.1038/203629a0

Holtzman, B. K., Kohlstedt, D. L., Zimmerman, M. E., Heidelbach, F., Hiraga, T., & Hustoft, J. (2003). Melt segregation and strain partitioning: Implications for seismic anisotropy and mantle flow. *Science*, *301*(5637), 1227–1230. https://doi.org/10.1126/science.1087132

Hudson, J. A. (1981). Wave speeds and attenuation of elastic waves in material containing cracks. *Geophysical Journal International*, *64*(1), 133–150. https://doi.org/10.1111/j.1365-246X.1981.tb02662.x

Jung, H., & Karato, S. (2001). Water-induced fabric transitions in olivine. *Science*, *293*(5534), 1460–1463. https://doi.org/10.1126/science.1062235

Kaminski, E., & Ribe, N. M. (2002). Timescales for the evolution of seismic anisotropy in mantle flow. *Geochemistry, Geophysics, Geosystems*, *3*(8), 1051. https://doi.org/10.1029/2001GC000222

Keen, C. E., & Barrett, D. L. (1971). A measurement of seismic anisotropy in the Northeast Pacific. *Canadian Journal of Earth Sciences*, *8*(9), 1056–1064. https://doi.org/10.1139/e71-092

Keen, C. E., & Tramontini, C. (1970). A seismic refraction survey on the Mid-Atlantic Ridge. *Geophysical Journal International*, *20*(5), 473–491. https://doi.org/10.1111/j.1365-246X.1970.tb06087.x

Kelemen, P. B., Dick, H. J. B., & Quick, J. E. (1992). Formation of harzburgite by pervasive melt/rock reaction in the upper mantle. *Nature*, *358*(6388), 635–641. https://doi.org/10.1038/358635a0

Korenaga, J. (2007). Thermal cracking and the deep hydration of oceanic lithosphere: A key to the generation of plate tectonics? *Journal of Geophysical Research*, *112*, B05408. https://doi.org/10.1029/2006JB004502

Langmuir, C. H., Klein, E. M., & Plank, T. (1992). Petrological systematics of mid-ocean ridge basalts: Constraints on melt generation beneath ocean ridges. In J. P. Morgan, D. K. Blackman, & J. M. Sinton (Eds.), *Mantle Flow and Melt Generation at Mid-Ocean Ridges* (pp. 183–280). American Geophysical Union. https://doi.org/10.1029/GM071p0183

Lin, P.-Y. P., Gaherty, J. B., Jin, G., Collins, J. A., Lizarralde, D., Evans, R. L., & Hirth, G. (2016). High-resolution seismic constraints on flow dynamics in the oceanic asthenosphere. *Nature*, *535*(7613), 538–541. https://doi.org/10.1038/nature18012

Mainprice, D. (2015). Seismic anisotropy of the deep Earth from a mineral and rock physics perspective. In *Treatise on Geophysics* (pp. 487–538). Elsevier. https://doi.org/10.1016/B978-0-444-53802-4.00044-0

Mainprice, D., Barruol, G., & Ismaïl, W. B. (2000). The seismic anisotropy of the Earth's mantle: From single crystal to polycrystal. In S.-I. Karato, A. Forte, R. Liebermann, Guysters, & L. Stixrude (Eds.), *Earth's Deep Interior: Mineral Physics and Tomography From the Atomic to the Global Scale* (pp. 237–264). Washington, DC: American Geophysical Union. https://doi.org/10.1029/GM117p0237

Meglis, I. L., Greenfield, R. J., Engelder, T., & Graham, E. K. (1996). Pressure dependence of velocity and attenuation and its relationship to crack closure in crystalline rocks. *Journal of Geophysical Research*, *101*(B8), 17,523–17,533. https://doi.org/10.1029/96JB00107

Mishra, J. K., & Gordon, R. G. (2016). The rigid-plate and shrinking-plate hypotheses: Implications for the azimuths of transform faults. *Tectonics*, *35*, 1827–1842. https://doi.org/10.1002/2015TC003968

Morris, G. B., Raitt, R. W., & Shor, G. G. (1969). Velocity anisotropy and delay-time maps of the mantle near Hawaii. *Journal of Geophysical Research*, *74*(17), 4300–4316. https://doi.org/10.1029/JB074i017p04300

Nicolas, A., Boudier, F., & Boullier, A. M. (1973). Mechanisms of flow in naturally and experimentally deformed peridotites. *American Journal of Science*, *273*(10), 853–876. https://doi.org/10.2475/ajs.273.10.853

Nicolas, A., & Christensen, N. I. (1987). Formation of anisotropy in upper mantle peridotites—A review. In K. Fuchs & C. Froidevaux (Eds.), *Composition, Structure and Dynamics of the Lithosphere-Asthenosphere System* (pp. 111–123). Washington, DC: American Geophysical Union. https://doi.org/10.1029/GD016p0111

Nishizawa, O. (1982). Seismic velocity anisotropy in a medium containing oriented cracks—Transversely isotropic case. *Journal of Physics of the Earth*, *30*(4), 331–347. https://doi.org/10.4294/jpe1952.30.331

Qi, C., Hansen, L. N., Wallis, D., Holtzman, B. K., & Kohlstedt, D. L. (2018). Crystallographic preferred orientation of olivine in sheared partially molten rocks: The source of the "A–C switch". *Geochemistry, Geophysics, Geosystems.* https://doi.org/10.1002/2017GC007309, *19*(2), 316–336.

Raitt, R. W., Shor, G. G., Francis, T. J. G., & Morris, G. B. (1969). Anisotropy of the Pacific upper mantle. *Journal of Geophysical Research*, *74*(12), 3095–3109. https://doi.org/10.1029/JB074i012p03095

Ribe, N. M. (1992). On the relation between seismic anisotropy and finite strain. *Journal of Geophysical Research*, *97*(B6), 8737–8747. https://doi.org/10.1029/92JB00551

Ringwood, A. E. (1958). The constitution of the mantle—III consequences of the olivine-spinel transition. *Geochimica et Cosmochimica Acta*, *15*(3), 195–212. https://doi.org/10.1016/0016-7037(58)90057-7

Russell, J. B., Gaherty, J. B., Lin, P.-Y. P., Lizarralde, D., Collins, J. A., Hirth, G., & Evans, R. L. (2019). High-resolution constraints on pacific upper mantle petrofabric inferred from surface-wave anisotropy. *Journal of Geophysical Research: Solid Earth*, *124*. https://doi.org/10.1029/2018JB016598

Ryan, W. B. F., Carbotte, S. M., Coplan, J. O., O'Hara, S., Melkonian, A., Arko, R., et al. (2009). Global multi-resolution topography synthesis. *Geochemistry, Geophysics, Geosystems*, *10*, Q03014. https://doi.org/10.1029/2008GC002332

Sandwell, D., & Fialko, Y. (2004). Warping and cracking of the Pacific plate by thermal contraction. *Journal of Geophysical Research*, *109*, B10411. https://doi.org/10.1029/2004JB003091

Sasajima, R., & Ito, T. (2017). Anisotropic horizontal thermal contraction of young oceanic lithosphere inferred from stress release due to oceanic intraplate earthquakes. *Tectonics*, *36*, 1988–2021. https://doi.org/10.1002/2017TC004680

Seton, M., Müller, R. D., Zahirovic, S., Gaina, C., Torsvik, T., Shephard, G., et al. (2012). Global continental and ocean basin reconstructions since 200 Ma. *Earth-Science Reviews*, *113*(3–4), 212–270. https://doi.org/10.1016/j.earscirev.2012.03.002

Shearer, P. M., & Orcutt, J. (1985). Anisotropy in the oceanic lithosphere—Theory and observations from the Ngendei seismic refraction experiment in the South-West Pacific. *Geophysical Journal of the Royal Astronomical Society*, *80*(2), 493–526. https://doi.org/10.1111/j.1365-246X.1985.tb05105.x

Shearer, P. M., & Orcutt, J. A. (1986). Compressional and shear wave anisotropy in the oceanic lithosphere—The Ngendei seismic refraction experiment. *Geophysical Journal International*, *87*(3), 967–1003. https://doi.org/10.1111/j.1365-246X.1986.tb01979.x

Shimamura, H. (1984). Anisotropy in the oceanic lithosphere of the North-Western Pacific Basin. *Geophysical Journal International*, *76*(1), 253–260. https://doi.org/10.1111/j.1365-246X.1984.tb05042.x

Shintaku, N., Forsyth, D. W., Hajewski, C. J., & Weeraratne, D. S. (2014). *Pn* anisotropy in Mesozoic western Pacific lithosphere. *Journal of Geophysical Research: Solid Earth*, *119*, 3050–3063. https://doi.org/10.1002/2013JB010534

Skemer, P., & Hansen, L. N. (2016). Inferring upper-mantle flow from seismic anisotropy: An experimental perspective. *Tectonophysics*, *668-669*, 1–14. https://doi.org/10.1016/j.tecto.2015.12.003

Skemer, P., Warren, J. M., & Hirth, G. (2012). The influence of deformation history on the interpretation of seismic anisotropy. *Geochemistry, Geophysics, Geosystems*, *13*, Q03006. https://doi.org/10.1029/2011GC003988

Snydsman, W. E., Lewis, B. T. R., & McClain, J. (1975). Upper mantle velocities on the northern Cocos plate. *Earth and Planetary Science Letters*, *28*(1), 46–50. https://doi.org/10.1016/0012-821X(75)90072-2

Stixrude, L., & Lithgow-Bertelloni, C. (2005). Mineralogy and elasticity of the oceanic upper mantle: Origin of the low-velocity zone. *Journal of Geophysical Research*, *110*(B3). https://doi.org/10.1029/2004JB002965

Thomsen, L. (1995). Elastic anisotropy due to aligned cracks in porous rock. *Geophysical Prospecting*, *43*(6), 805–829. https://doi.org/10.1111/j.1365-2478.1995.tb00282.x

Toomey, D. R., Jousselin, D., Dunn, R. A., Wilcock, W. S. D., & Detrick, R. S. (2007). Skew of mantle upwelling beneath the East Pacific rise governs segmentation. *Nature*, *446*(7134), 409–414. https://doi.org/10.1038/nature05679

Turner, F. J. (1942). Preferred orientation of olivine crystals in peridotites, with special reference to New Zealand examples. *Transactions and Proceedings of the Royal Society of New Zealand*, *72*(3), 280–300.

VanderBeek, B. P., & Toomey, D. R. (2017). Shallow mantle anisotropy beneath the Juan de Fuca plate. *Geophysical Research Letters*, *44*, 11,382–11,389. https://doi.org/10.1002/2017GL074769

VanderBeek, B. P., Toomey, D. R., Hooft, E. E. E., & Wilcock, W. S. D. (2016). Segmentation of mid-ocean ridges attributed to oblique mantle divergence. *Nature Geoscience*, *9*(8), 636–642. https://doi.org/10.1038/ngeo2745

Verma, R. K. (1960). Elasticity of some high-density crystals. *Journal of Geophysical Research*, *65*(2), 757–766. https://doi.org/10.1029/JZ065i002p00757

Zhang, S., & Karato, S. (1995). Lattice preferred orientation of olivine aggregates deformed in simple shear. *Nature*, *375*(6534), 774–777. https://doi.org/10.1038/375774a0

Zhong, X., Frehner, M., Kunze, K., & Zappone, A. (2014). A novel EBSD-based finite-element wave propagation model for investigating seismic anisotropy: Application to Finero peridotite, Ivrea-Verbano zone, northern Italy. *Geophysical Research Letters*, *41*, 7105–7114. https://doi.org/10.1002/2014GL060490